Wave amplitude gain within wedge waveguides through scattering by simple obstacles

A. L. Azevedo ⊙,[*] A. C. Maioli ⊙,[*,†] F. Teston, M. R. Sales ⊙,[‡] F. M. Zanetti, and M. G. E. da Luz ⊙[§]

Departamento de Física, Universidade Federal do Paraná, Curitiba-PR, 81531-980, Brazil

Wave confinement, e.g., in waveguides, gives rise to a huge number of distinct phenomena. Among them, amplitude gain is a recurrent and relevant effect in undulatory processes. Using a general purpose protocol to solve wave equations, the boundary wall method, we demonstrate that for relatively simple geometries, namely, a few leaky or opaque obstacles inside a θ wedge waveguide (described by the Helmholtz equation), one can obtain a considerable wave amplification in certain spatially localized regions of the system. The approach relies on an expression for the wedge waveguide exact Green's function in the case of $\theta = \pi/M$ ($M = 1, 2, \ldots$), derived through the method of images allied to group theory concepts. The formula is particularly amenable to numerical calculations, greatly facilitating simulations. As an interesting by-product of the present framework, we are able to obtain the eigenstates of certain closed shapes (billiards) placed within the waveguide, as demonstrated for triangular structures. Finally, we briefly discuss possible concrete realizations for our setups in the context of matter and electromagnetic (for some particular modes and conditions) waves.

I. INTRODUCTION

One cannot emphasize enough the richness of phenomena emerging from confinement of either electromagnetic [1–5] or matter [6–9] waves [10,11]. The confinement can be total, realized by resonance cavities, quantum dots, quantum billiards, etc., or partial, such as taking place along a certain particular direction, usually achieved by means of waveguide-like structures; for quantum problems see, e.g., Ref. [12], a complete compendium detailing many instances of bound and scattering states on waveguides. In particular, wedge waveguides [Fig. 1(a)] have been used to study many physical processes (for representative examples refer to [13–21]). Further, they constitute useful systems for the development of theoretical and mathematical methods, like in the calculation of quantum time-dependent propagators and energy-domain Green's functions [22–31].

Among distinct undulatory effects, interference, or more specifically constructive interference, can give rise to appreciable localized amplification: in certain regions of space the scattered wave ψ presents a much higher amplitude than that of the incident φ, caused by properly shaped and placed scatters. This type of effect has great interest both for being relatively common in nature and due to the many potential applications [32–39]. In such a context, wedge waveguides seem to be very suitable to attain interference and amplitude gain (or amplification) [2,16–18], like in some clever setups for lasing [15,17,33,34,40,41].

The aforementioned studies require convenient approaches [42–44] to predict and quantify the unfolding of wave amplification in waveguides and/or cavities and moreover allowing one to treat distinct shapes and properties for the scatters in the interior of these structures. Also, they should be practical enough to permit a searching for setups (ideally simple) leading to the sought amplitude gain. For instance, amplitude enhancement can be attained through many scatters randomly distributed [45–48]. However, eventually it might be possible to obtain similar amplifications, at least in some spatial domain of the system, from a smaller number of scatters by fine tuning their exact locations. Certainly, schemes amenable to this kind of analysis would be very welcome.

The boundary wall method (BWM) [49–51] is a protocol developed to treat wave equations, such as Helmholtz's, in any spatial dimension and for different boundary conditions, including leaking walls; see, e.g., [52]. It leads to the outside scattering and the inside eigenmodes (in the case of closed shapes) solutions for arbitrary structures. The BWM has been used to investigate many different aspects of, e.g., mesoscopic and nanoscopic quantum devices [53–58], photonic crystals [59,60], and potential switchers for logical operators [51,61].

One of the advantages of BWM relates to its great versatility in exploring the physical consequences of changes in the geometry and features (like permeability) of a basic structure shape. But despite the BWM generality and flexibility, the original formulation would be numerically expensive if employed in systems formed by long (or even more difficulty, infinite) waveguides. However, recently an extension of the BWM has been proposed [62], making it very handy for problems involving waveguide architectures. Technically, the key idea is rather simple. One should assume the usual BWM basic equations to address the scattering of obstacles in the waveguide interior, nonetheless rewriting such equations in
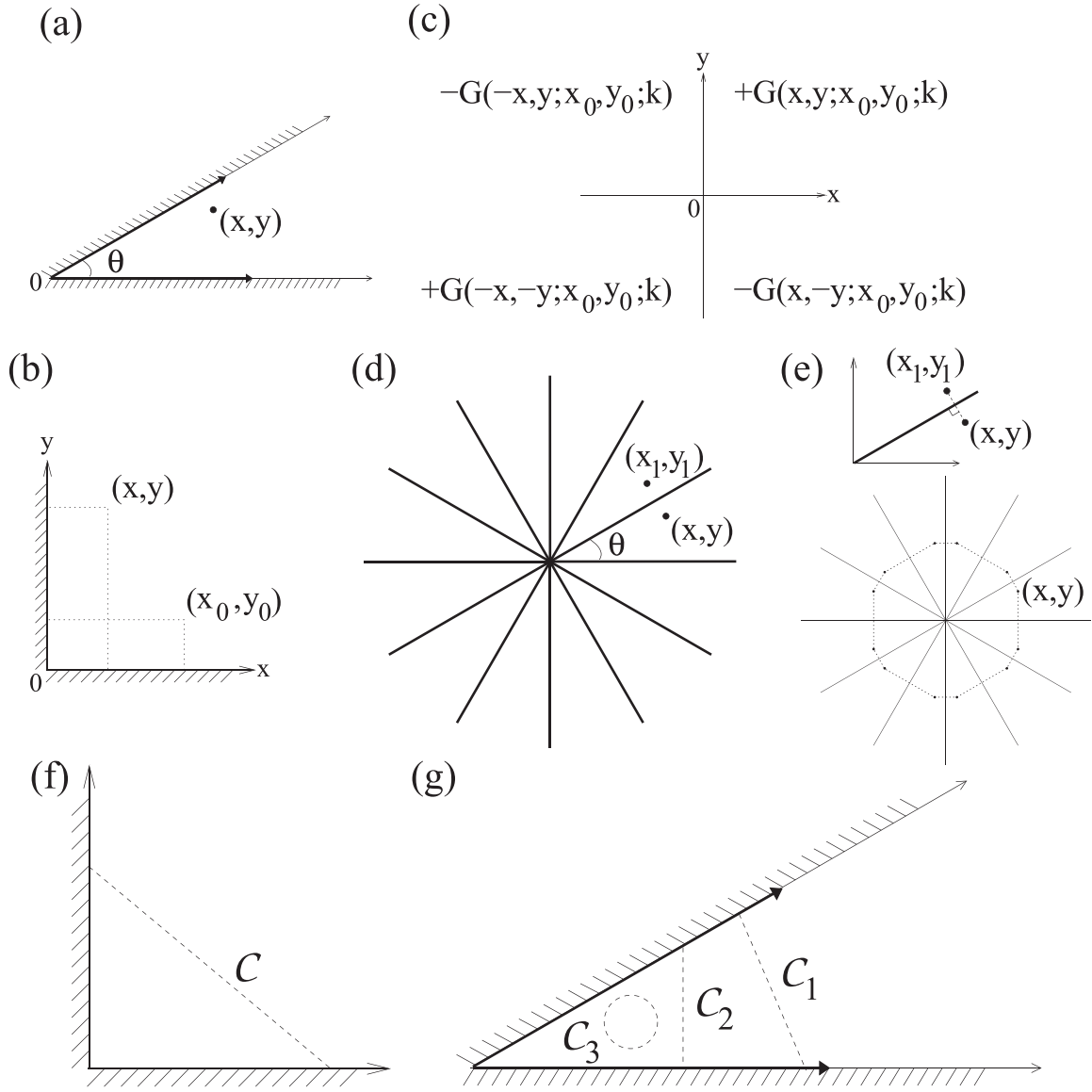

FIG. 1. (a) Schematics of the wedge waveguide considered in this work. (b) The case of $\theta = \pi/2$. (c) The method of images construction for $\theta = \pi/2$. Each shown G represents the expression for the Green's function in the 2D free space with the signals of x, y changed as indicated. The G's with modified x, y are then specular "images" of the Green's function in the first quadrant through the planes $x = 0$ and $y = 0$. The $\pm$ in front of the G's are the coefficients α_l defined in the paper. (d) The lines $l = 0, 1, \ldots, 2M - 1$ (with M a positive integer) form a starlike pattern in the plane. The $\theta = \pi/M$ wedge waveguide is delimited by the lines 0 and 1. (e) The specular image of a point within the waveguide with respect to the line 1 (top) and the successive specular images of this point about all the lines of the starlike structure of (d) (bottom). (f) With the help of parts of the wedge waveguide walls, a proper located segment of line wall $\mathcal{C}$ forms a billiard shape, as a right triangular billiard for the $\theta = \pi/4$ wedge waveguide. (g) For an acute wedge, examples of different walls $\mathcal{C}$ which can be placed inside the waveguide.

terms of the Green's function G of the waveguide of interest instead of a free Green's function.

Our purpose in the present contribution is twofold. First, we derive an exact expression for the Green's function G_θ of a bidimensional (2D) θ wedge waveguide in the case of $\theta = \pi/M$ ($M = 1, 2, \ldots$), which is much easier to work with numerically than other more common formulas in the literature. Although the final expression cannot be extended to an arbitrary waveguide angle θ, for the applications we shall discuss, this family of θ's already suffices. Second, considering this G_θ and the BWM, we investigate relatively simple

leaky and opaque structures which once introduced near the waveguide tip or vertex do lead to significant amplification in the vicinity of such region. We also introduce ways to characterize the degree of gain in all these cases. As a positive side effect of the method, one can also calculate the eigenstates of triangular billiards using wedge waveguides.

We focus in two dimensions, the x-y plane, since our aim is to examine in general terms the effect phenomenology rather than solving actual situations, which would demand specific details like the waveguide thickness. Nonetheless, we observe that if along the z direction the wedge waveguide and

inner structures are limited by two parallel planes, the corresponding z modes should be given by usual combinations of trigonometric functions (of course, depending on the boundary conditions). Hence, the essential physics would lie in two dimensions. Furthermore, we discuss the Helmholtz equation, which in principle is associated to matter waves. But in the 2D case, electromagnetic waves can be described by scalar fields (as for TEM modes) obeying the Helmholtz equation—in the context of the BWM see, e.g., Refs. [56,59,60]. In this way, the present results should be of interest to a broad range of undulatory processes.

The paper is organized as the following. Since a vast literature on the BWM exists, in Sec. II we review just the main principles and the fundamental equations related to the approach. In Sec. III, using a combination of the method of images with group theory (considering the Dihedral point group), we obtain the Green's function for a $\theta = \pi/M$ wedge waveguide. We validate the good numerical efficiency of the BWM allied to wedge waveguides analyzing triangular billiards in Sec. IV. In Sec. V we show how to achieve amplitude gain around the waveguide vertex by supposing either (i) a leak bulkhead (in the format of an arc of circle) or (ii) two permeable circles, placed near the waveguide tip. We determine the level of amplification by calculating the resulting scattering solutions from such obstacles. Discussion and final remarks are drawn in Sec. VI. In particular, a few distinct possible concrete applications for our framework are briefly commented. To facilitate the reading, some important derivations and results are left to Appendixes.

II. A BRIEF OVERVIEW OF THE BOUNDARY WALL METHOD

A comprehensive description of the BWM, including details about its general features, applicability and numerical implementation can be found in [49–51]. Further, a complete mathematical formulation for the BWM in the context of waveguide-like systems has been developed in [62]. Thus, below we just highlight the method essential aspects.

Assume V to be the internal region of a semi-infinite waveguide, as our θ wedge case in Fig. 1(a). We denote by ∂V the frontiers (borders) of this infinite region V. For the Helmholtz differential operator $\mathcal{H}_{\mathbf{r}}(k) = \nabla_{\mathbf{r}}^2 + k^2$ defined on V (with k the wavenumber and the system constants such that in arbitrary units $E = k^2$), suppose we know $G_V(\mathbf{r}; \mathbf{r}_0; k)$ and $\varphi(\mathbf{r}; k)$, such that

$$\mathcal{H}_{\mathbf{r}}(k) G_V(\mathbf{r}; \mathbf{r}_0; k) = \delta(\mathbf{r} - \mathbf{r}_0),$$
$$\mathcal{H}_{\mathbf{r}}(k) \varphi(\mathbf{r}; k) = 0,$$
$$G_V(\mathbf{r}; \mathbf{r}_0; k)|_{\mathbf{r} \in \partial V} = \varphi(\mathbf{r}; k)|_{\mathbf{r} \in \partial V} = 0. \quad (1)$$

Now, suppose an arbitrary structure—open or closed, connected or disconnected—of frontiers delimited by $\mathcal{C}$ (for explicit examples, see the following sections). By placing the structure in the interior of the waveguide, denoting by $\mathbf{r}(t)$ the vector position of a point t ($t_i \leqslant t \leqslant t_f$) on its contour $\mathcal{C}$ and taking φ as any wave satisfying Eq. (1), the whole system proper stationary scattering solution $\psi(\mathbf{r}; k)$ is given by (for $\mathbf{r}$

any vector position in V)

$$\psi(\mathbf{r}; k) = \varphi(\mathbf{r}; k) + \gamma \int_{t_i}^{t_f} \int_{t_i}^{t_f} dt'' \, dt' \, G_V(\mathbf{r}; \mathbf{r}(t''); k)$$
$$\times T_\gamma(t'', t'; k) \, \varphi(\mathbf{r}(t'); k). \quad (2)$$

Here $T_\gamma(t'', t'; k)$ is the problem T matrix, whose series expansion reads

$$T_\gamma(t'', t'; k) = \delta(t'' - t') + \sum_{j=1}^{\infty} T_\gamma^{(j)}(t'', t'; k), \quad (3)$$

for

$$T_\gamma^{(j)}(t'', t'; k) = \gamma^j \int_{t_i}^{t_f} dt_1 \cdots dt_{j-1} \, G_V(\mathbf{r}(t''); \mathbf{r}(t_{j-1}); k)$$
$$\times G_V(\mathbf{r}(t_{j-1}); \mathbf{r}(t_{j-2}); k) \ldots G_V(\mathbf{r}(t_2);$$
$$\times \mathbf{r}(t_1); k) \, G_V(\mathbf{r}(t_1); \mathbf{r}(t'); k). \quad (4)$$

These equations could easily be extended to the situation where the parameter γ depends on the t's over $\mathcal{C}$ [49], but we are not going to discuss this case in the present contribution. The quantity γ represents the structure $\mathcal{C}$ permeability. Indeed, for a plane wave of wavenumber k incident perpendicular to a point on $\mathcal{C}$, it has the probabilities $P_t = 4k^2/(4k^2 + \gamma^2)$ and $1 - P_t$ to be, respectively, transmitted through and reflected from it. For $\gamma = 0$, obviously there is no obstacle, and for $\gamma \to \infty$ we have a hard wall $\mathcal{C}$, leading to Dirichlet boundary conditions for ψ over $\mathcal{C}$.

As for the limit $\gamma \to \infty$, by setting $T(t'', t'; k) = -\lim_{\gamma \to \infty} \gamma \, T_\gamma(t'', t; k)$, one can prove that [50]

$$\delta(t'' - t') = \int_{t_i}^{t_f} dt \, T(t'', t; k) \, G_V(\mathbf{r}(t); \mathbf{r}(t'); k)$$
$$= \int_{t_i}^{t_f} dt \, G_V(\mathbf{r}(t''); \mathbf{r}(t); k) \, T(t, t'; k), \quad (5)$$

with Eq. (2) then reading

$$\psi(\mathbf{r}; k) = \varphi(\mathbf{r}; k) - \int_{t_i}^{t_f} \int_{t_i}^{t_f} dt'' \, dt' \, G_V(\mathbf{r}; \mathbf{r}(t''); k)$$
$$\times T(t'', t'; k) \, \varphi(\mathbf{r}(t'); k). \quad (6)$$

The wavefunction ψ in Eq. (6) has a remarkable property if $\mathcal{C}$ is a closed shape. For the external region of $\mathcal{C}$, ψ is the stationary scattering solution for an incoming φ scattered off by $\mathcal{C}$. But for the internal region of $\mathcal{C}$, provided that φ does meet some simple general requirements (refer to [50]), if k_n is the problem nth eigenwavenumber, then for $k \neq k_n$ we have an identically null ψ, whereas for $k = k_n$ we have that $\psi = \psi_n$ is the corresponding correct inner eigenstate.

Finally, the BWM numerical construction is relatively straightforward. One considers discretized versions of the T matrix, either for T_γ or for T, by dividing the full $\mathcal{C}$ into N "pieces" (or segments if in two dimensions), so that T becomes a matrix of order $N \times N$. With such a quantity, the integrals for ψ are solved by simple quadratures (for the full protocol see Refs. [50,51,63]). Also, to look for the k_n's for the case of $\mathcal{C}$ a billiard, one just numerically computes the discrete T and then analyzes its behavior as function of k.

The emergence of certain patterns for the matrix elements at particular k's (basically high peaks for certain off-diagonal terms) indicates the resonances [49,50].

These standard procedures will be the ones followed in all our calculations in the present work.

III. THE SYSTEM: THE $\theta = \pi/M$ ($M = 1, 2, \ldots$) WEDGE WAVEGUIDES

For a θ wedge waveguide, the spatial domain V comprises its inner region, depicted in Fig. 1(a). In polar coordinates (ρ, ϕ), V corresponds to $\rho > 0$ and $0 < \phi < \theta$. Note that in Cartesian coordinates, the waveguide borders are the semi-infinite lines $\{x \geqslant 0, y = 0\}$ and $\{x \geqslant 0, y = \tan[\theta] x\}$. We denote the system retarded $(+)$ and advanced $(-)$ Green's functions in V as $G_{\text{wedge}}^{(\pm)}(\rho, \phi; \rho_0, \phi_0; k)$, satisfying Dirichlet boundary conditions, namely, $G_{\text{wedge}}^{(\pm)}(\rho, \phi; \rho_0, \phi_0; k) = 0$ for ϕ and/or ϕ_0 equal to either 0 or θ. The exact expression for $G_{\text{wedge}}^{(\pm)}$ was obtained more than a century ago [64], with a very instructive recent derivation given in [65]. We also mention that $G_{\text{wedge}}^{(\pm)}$ follows rather directly from the general method discussed in [62]. For $\rho_>$ $(\rho_<)$ representing the greater (smaller) between ρ and ρ_0 and for J_ν $(H_\nu^{(\pm)})$ being the Bessel function [Hankel function of first $(+)$ or $(-)$ second kind] of order ν [66,67], one finds (for completeness, a deduction is presented in the Appendix A)

$$G_{\text{wedge}}^{(\pm)}(\rho, \phi; \rho_0, \phi_0; k) = \mp i\frac{\pi}{2} \sum_{n=1}^{\infty} \varphi_n^{(\theta)}(\phi)\, \varphi_n^{(\theta)}(\phi_0)$$
$$\times J_{n\frac{\pi}{\theta}}(k\rho_<)\, H_{n\frac{\pi}{\theta}}^{(\pm)}(k\rho_>), \quad (7)$$

$$\varphi_n^{(\theta)}(z) = \sqrt{\frac{2}{\theta}} \sin\left[\frac{n\pi z}{\theta}\right]. \quad (8)$$

A caveat of Eq. (7) is that it is not so easy to work with numerically. Indeed, as discussed in [65] (see, e.g., its Sec. 6.1), in diffraction theory usually formulas like the above one are of practical usage only in the far-field limit (i.e., large ρ). Nevertheless, depending on the type of application one has in mind, the exact value of the angle (or aperture) θ might not be critical, provided θ belongs to a suitable interval. This has prompted the development of different dedicated protocols to compute the Green's function and the corresponding scalar scattering field $\psi(\mathbf{r})$, considering particular θ's, e.g., θ/π rational [68,69]. For a comprehensive review on the topic, including discussions about modern rigorous approaches to solve different waveguides see, for instance, Ref. [70].

Motivated by the above considerations, next we derive a much simpler exact expression for the Green's function than that in Eq. (7), being valid for any $\theta = \pi/M$ ($M = 1, 2, \ldots$). Then, based on such a formula and the modified BWM proposed in [62], we shall analyze distinct scattering problems in wedge waveguides. Hereafter we will consider only the outgoing $G_{\text{wedge}}^{(+)}$ case.

A. The exact Green's function $G_{\pi/M}^{(+)}$

Our starting point is the Green's function for the 2D free space, given by $G_0(\mathbf{r}, \mathbf{r}_0; k) = -(i/4)H_0^{(+)}(k|\mathbf{r} - \mathbf{r}_0|)$ [66,71].

From it, we consider the method of images applied to G_0, so to obtain the exact $G_{\theta = \pi/M}^{(+)}$.

The method of images is a common and powerful calculation protocol in many branches of physics [71]. In the context of Green's functions, its implementation can be summarized as the following. Suppose one seeks G for the (differential) operator $\hat{\mathfrak{D}}$ in a certain region $V \subset \mathbb{R}^N$, with Dirichlet boundary conditions at the frontiers $\mathcal{C}_V$ of V. Assume $G(\mathbf{r}; \mathbf{r}_0)$ the Green's function of the full free space. Hence $\hat{\mathfrak{D}}\, G(\mathbf{r}; \mathbf{r}_0) = \delta(\mathbf{r} - \mathbf{r}_0)$ for any $\mathbf{r}$ and $\mathbf{r}_0$ in $\mathbb{R}^N$ (here $\hat{\mathfrak{D}}$ acts on the variable $\mathbf{r}$). The main idea is then try to find a minimal number of functions $f_l(\mathbf{r})$ and constants α_l, $l = 1, 2, \ldots, L$, such that for all $\mathbf{r}, \mathbf{r}_0 \in V$: (i) $\hat{\mathcal{D}}\, G(f_l(\mathbf{r}); \mathbf{r}_0) = 0$ for any l and (ii) $G_V(\mathbf{r}; \mathbf{r}_0) \equiv G(\mathbf{r}; \mathbf{r}_0) + \sum_{l=1}^{L} \alpha_l\, G(f_l(\mathbf{r}); \mathbf{r}_0)$ identically vanishes for all $\mathbf{r} \in \mathcal{C}_V$. In this case, G_V is the correct Green function in V. The existence or not of the set $\{(f_l, \alpha_l)\}$ will strongly depend on the symmetries of the problem, which are often associated with specular reflections (so "images") about certain directions in V [72]. Of course, our interest is in the Helmholtz equation, or $\hat{\mathfrak{D}} = \mathcal{H}_{\mathbf{r}}(k) = \nabla_{\mathbf{r}}^2 + k^2$.

To gain some insight into the procedure, we begin with the simple example of $\theta = \pi/2$. The region of interest, V, is the first quadrant of the 2D plane depicted in Fig. 1(b). For the free 2D space, G is the previously mentioned Hankel function of first kind of order 0, with the argument $k\,|\mathbf{r} - \mathbf{r}_0| = k\sqrt{(x - x_0)^2 + (y - y_0)^2}$. For $\mathbf{r} = (x, y)$, let us choose f_l and α_l ($l = 1, 2, 3$) as $f_1((x, y)) = (-x, y)$, $f_2((x, y)) = (-x, -y)$, $f_4((x, y)) = (x, -y)$ and $\alpha_1 = \alpha_3 = -1$, $\alpha_2 = 1$. Considering the sum (ii) above and assuming $\mathbf{r}$ and $\mathbf{r}_0$ in the first quadrant, regarding $\mathbf{r}$ we have that $\alpha_l\, G(f_l(\mathbf{r}); \mathbf{r}_0)$ lies in the second, third, and fourth quadrants for l equal, respectively, to 1, 2, and 3, as schematically illustrated in Fig. 1(c). Due to the form of the f_l's, we readily find that the sum of the four G's represented in Fig. 1(c) identically vanishes at $x = 0$ and $y = 0$. Once $\mathbf{r}$ and $\mathbf{r}_0$ are in the first quadrant, $f_l(\mathbf{r}) - \mathbf{r}_0$ cannot be null. Further, it is easy to show that $\nabla_{\mathbf{r}}^2 = \nabla_{f_l(\mathbf{r})}^2$. Therefore, the previous condition (i) is also observed, and thus the sum of the G's in Fig. 1(c) leads to the exact Green function $G_{\pi/4}^{(+)}$ for the 90° wedge waveguide.

The case $\theta = \pi$ is even simpler since the boundary conditions demand $G_\pi^{(+)}$ to be null just for $y = 0$. Taken into account that in the upper half-plane, where $G_\pi^{(+)}$ is defined, the y component of $\mathbf{r}$ and $\mathbf{r}_0$ is non-negative, we need only a single f, with $f_1((x, y)) = (x, -y)$ and $\alpha_1 = -1$. So one directly gets that in this case (i) and (ii) are satisfied by writing [for $\mathbf{r} = (x, y)$, $\mathbf{r}_0 = (x_0, y_0)$ and y, y_0 non-negative: first and second quadrants]

$$G_\pi^{(+)}(\mathbf{r}; \mathbf{r}_0; k) = -\frac{i}{4}H_0^{(+)}(k\,|\mathbf{r} - \mathbf{r}_0|)$$
$$+ \frac{i}{4}H_0^{(+)}(k\,|(x, -y) - \mathbf{r}_0|). \quad (9)$$

For sake of comparison, the above expression is also deduced from the general Eq. (7) in Appendix B.

We now address the general situation of $\theta = \pi/M$, with M any positive integer. The previous two examples correspond to $M = 2$ and $M = 1$. For $M = 3, 4, 5, 6, \ldots$, we have θ equals, respectively, to 60°, 45°, 36°, 30°, ... To determine the f_l's, suppose semi-infinite lines labeled counterclockwise as l and

defined by $\rho > 0$ and $\phi = l\,\theta$ with $l = 0, 1, 2, \ldots, 2M - 1$. They form the pattern displayed in Fig. 1(d), for which the wedge waveguide is the region delimited by the lines $l = 0$ and $l = 1$. Remarkably, such a structure corresponds to all the $2M$ symmetry axes of the Dihedral group D_M of a regular polygon of M sides [73]. The Dihedral group has a representation in terms of reflections S and rotations R matrices in the form [74] ($l = 0, \ldots, M - 1$)

$$S_{l\theta} = \begin{pmatrix} \cos[2\,l\,\theta] & \sin[2\,l\,\theta] \\ \sin[2\,l\,\theta] & -\cos[2\,l\,\theta] \end{pmatrix},$$

$$R_{l\theta} = \begin{pmatrix} \cos[2\,l\,\theta] & -\sin[2\,l\,\theta] \\ \sin[2\,l\,\theta] & \cos[2\,l\,\theta] \end{pmatrix}. \tag{10}$$

As for the action of the S's and R's in Eq. (10), first for any point $\mathbf{r}$ in the region between the lines l and $l + 1$, the specular image of $\mathbf{r}$ about $l + 1$ is given by $S_{(l+1)\theta}(\mathbf{r})$ [74]. Thus, successive reflections of an initial $\mathbf{r}$ by the S'_ls generate a closed loop, as schematically depicted in Fig. 1(e). Second, for $\mathbf{r}$ belonging to the line l, then $\mathbf{r}$ and $S_{l\theta}(\mathbf{r})$ coincide, whereas $S_{(l+1)\theta}(\mathbf{r})$ is on the line $l + 2$. And, third, $R_{l\theta}$ represents a rotation by an angle $2\,l\,\theta$. In this way, for $\mathbf{r}$ on the line l, it follows that $R_{l'\theta}(\mathbf{r})$ is on the line $l + 2\,l'$. Note that l is given in mod $2M$. Importantly, $\nabla^2_{\mathbf{r}} = \nabla^2_{\tilde{\mathbf{r}}}$ for $\tilde{\mathbf{r}} = S_{l\theta}(\mathbf{r})$ or $\tilde{\mathbf{r}} = R_{l\theta}(\mathbf{r})$. Thus, for all functions $\Theta(\tilde{\mathbf{r}})$ for which $(\nabla^2_{\tilde{\mathbf{r}}} + k^2)\,\Theta(\tilde{\mathbf{r}}) = 0$, $(\nabla^2_{\mathbf{r}} + k^2)\,\Theta(\tilde{\mathbf{r}}) = 0$ as well.

Now, to see how the above results can be employed in the method of images, consider the following. For an arbitrary $\mathbf{r} = (x, y)$ within the waveguide region [Fig. 1(d)] and for (x_1, y_1) its specular image with respect to line 1 [Fig. 1(e)] one has

$$S_\theta(\mathbf{r}) = S_\theta \begin{pmatrix} x \\ y \end{pmatrix} = \begin{pmatrix} x_1 \\ y_1 \end{pmatrix}. \tag{11}$$

Hence, if $\mathbf{r} = (x, y)$ is on line 1 (i.e., $y = x \tan[\theta]$), we have $(x_1, y_1) = (x, y)$. Consequently, for an arbitrary function Θ, the sum $T_2 = \Theta(\mathbf{r}) - \Theta(S_\theta(\mathbf{r}))$ identically vanishes for $\mathbf{r}$ along line 1. On the other hand, for $\mathbf{r}$ on the line 0, $S_\theta(\mathbf{r})$ is on line 2. Thus, T_2 is not necessarily null along line 0. In its

turn, the sum $T_4 = \Theta(\mathbf{r}) - \Theta(S_\theta(\mathbf{r})) + \Theta(R_\theta(\mathbf{r})) - \Theta(S_0(\mathbf{r}))$ is always zero over line 0 once, in such case, $\Theta(S_\theta(\mathbf{r})) = \Theta(R_\theta(\mathbf{r}))$ and $\Theta(\mathbf{r}) = \Theta(S_0(\mathbf{r}))$. But for $\mathbf{r}$ belonging to line 1, $R_\theta(\mathbf{r})$ is on line 3 and $S_0(\mathbf{r})$ is on line $2M - 1$. So we cannot guarantee that $T_4 = 0$ over line 1 given that $\Theta(R_\theta(\mathbf{r})) - \Theta(S_0(\mathbf{r}))$ does not mandatorily cancels out. However, the idea is to keep including more terms in the construction of T_n, until a *finite* sum to consistently satisfy the Dirichlet boundary conditions along lines 0 and 1.

Actually, this is always possible because our S's and R's are in fact elements of the $\theta = \pi/M$ *finite* Dihedral group. Thus, starting from $\mathbf{r} = (x, y)$ in the wedge waveguide region, if we define ours $f_l(\mathbf{r}) = \mathbf{r}_l = (x_l, y_l)$ [refer to (i) and (ii) above] as the lth successive specular image through lines $1, 2, \ldots, l$ [Fig. 1(e)], we get

$$\mathbf{r}_l = S_{l\theta}(\mathbf{r}_{l-1}) = (S_{l\theta}\,S_{(l-1)\theta})(\mathbf{r}_{l-2})$$
$$= (S_{l\theta}\,S_{(l-1)\theta}\,S_{(l-2)\theta})(\mathbf{r}_{l-3}) = \cdots \tag{12}$$
$$= (S_{l\theta}\,S_{(l-1)\theta}\cdots S_{2\theta}\,S_\theta)(\mathbf{r}),$$

which from Eq. (10) yields after some manipulations

$$\mathbf{r}_l = f_l^{(D)}(\mathbf{r}) = S_{\frac{(l+1)}{2}\theta}(\mathbf{r}), \quad \text{if } l \text{ is odd},$$
$$\mathbf{r}_l = f_l^{(D)}(\mathbf{r}) = R_{\frac{l}{2}\theta}(\mathbf{r}), \qquad \text{if } l \text{ is even}. \tag{13}$$

Therefore, we finally can write the exact Green's function for the problem as [observing that $f_0^{(D)}(\mathbf{r}) = \mathbf{r}$ and setting $\alpha_l = (-1)^l$]

$$G_{\pi/M}^{(+)}(\mathbf{r}; \mathbf{r}_0; k) = -\frac{i}{4} \sum_{l=0}^{l=2M-1} (-1)^l\,H_0^{(+)}\big(k\,\big|f_l^{(D)}(\mathbf{r}) - \mathbf{r}_0\big|\big). \tag{14}$$

One could try to apply the same procedure for $\theta = p\,\pi/M$, with p and M relative primes and $p < 2M$. But in this case the angle θ does not divide the plane into an even number of equally spaced angular sectors. So the previous scheme cannot work.

As two examples, for $\theta = \pi/3$, i.e., a $60°$ wedge, if we define $x_\pm = \sqrt{3}\,(\sqrt{3}\,x_0 \pm y_0)$, $y_\pm = \sqrt{3}\,(\sqrt{3}\,y_0 \pm x_0)$, the corresponding exact Green's function reads

$$G_{\pi/3}^{(+)} = \frac{-i}{4}\{H_0^{(+)}[k\sqrt{(x - x_0)^2 + (y - y_0)^2}] - H_0^{(+)}[k\sqrt{(x - x_0)^2 + (y + y_0)^2 + x_- x - y_+ y}]$$
$$+ H_0^{(+)}[k\sqrt{(x - x_0)^2 + (y - y_0)^2 + x_- x + y_+ y}] - H_0^{(+)}[k\sqrt{(x - x_0)^2 + (y + y_0)^2 + x_+ x - y_- y}]$$
$$+ H_0^{(+)}[k\sqrt{(x - x_0)^2 + (y - y_0)^2 + x_+ x + y_- y}] - H_0^{(+)}[k\sqrt{(x - x_0)^2 + (y + y_0)^2}]\}. \tag{15}$$

Observe that as it should be, either for $y = 0$ or for $y = \sqrt{3}\,x$ the above expression identically vanishes.

For $\theta = \pi/4$ (or $45°$), defining $x_\pm = 2\,(x_0 \pm y_0)$, $y_\pm = 2\,(y_0 \pm x_0)$, then

$$G_{\pi/4}^{(+)} = \frac{-i}{4}\{H_0^{(+)}[k\sqrt{(x - x_0)^2 + (y - y_0)^2}] - H_0^{(+)}[k\sqrt{(x - x_0)^2 + (y - y_0)^2 + x_+ x + y_+ y}]$$
$$+ H_0^{(+)}[k\sqrt{(x - x_0)^2 + (y - y_0)^2 + x_+ x + y_- y}] - H_0^{(+)}[k\sqrt{(x + x_0)^2 + (y - y_0)^2}]$$
$$+ H_0^{(+)}[k\sqrt{(x + x_0)^2 + (y + y_0)^2}] - H_0^{(+)}[k\sqrt{(x - x_0)^2 + (y - y_0)^2 + x_- x + y_- y}]$$
$$+ H_0^{(+)}[k\sqrt{(x - x_0)^2 + (y - y_0)^2 + x_- x + y_+ y}] - H_0^{(+)}[k\sqrt{(x - x_0)^2 + (y + y_0)^2}]\}. \tag{16}$$

which likewise vanishes for $y = 0$ and $y = x$.

B. Plane wavelike solutions within the wedge waveguide

For later convenience, it is useful to derive a plane wavelike solution within the wedge waveguide. For so, we could use, e.g., the general (although a bit involved) technique in chapter 7 of Ref. [66]. Nonetheless, for our special values of $\theta = \pi/M$, it can be done in a simpler way.

For A^{T} denoting the transpose of the matrix A and recalling that S and R represent reflections and rotations, we have that $S_{l\theta}^{\mathrm{T}} = S_{l\theta}$ and $R_{l\theta}^{\mathrm{T}} = R_{2\pi - l\theta} = R_{(M-l)\theta}$. So, for any wavenumber vector $\mathbf{k}$ and position $\mathbf{r}$: $\mathbf{k} \cdot S_{l\theta}(\mathbf{r}) = S_{l\theta}(\mathbf{k}) \cdot \mathbf{r}$ and $\mathbf{k} \cdot R_{l\theta}(\mathbf{r}) = R_{(M-l)\theta}(\mathbf{k}) \cdot \mathbf{r}$. Further, by defining $\mathbf{k}_l = f_l^{(D)}(\mathbf{k})$ then $k^2 = |\mathbf{k}|^2 = |\mathbf{k}_l|^2$. Consequently, $\mathcal{N} \exp[i\,\mathbf{k}_l \cdot \mathbf{r}]$ solves the Helmholtz equation (of energy k^2) in the 2D free space. Finally, from the previous method of image analysis, we know that for an arbitrary function Θ, the sum $\sum_{l=0}^{l=2M-1} (-1)^l\,\Theta(\mathbf{k} \cdot f_l^{(D)}(\mathbf{r}))$ identically vanishes if $\mathbf{r}$ is on the borders of the π/M wedge waveguide. Thence, considering the previous definition of $f_l^{(D)}$, a valid plane wavelike solution for the inner region of our π/M wedge waveguide reads

$$
\begin{aligned}
\varphi(\mathbf{r}; \mathbf{k}) &= \mathcal{N} \sum_{l=0}^{2M-1} (-1)^l \exp\left[i\,\mathbf{k} \cdot f_l^{(D)}(\mathbf{r})\right] = \mathcal{N} \left\{ \sum_{l=0}^{M-1} \exp[i\,R_{(M-l)\theta}(\mathbf{k}) \cdot \mathbf{r}] - \sum_{l=1}^{M} \exp[i\,S_{l\theta}(\mathbf{k}) \cdot \mathbf{r}] \right\} \\
&= \mathcal{N} \left\{ \sum_{l=0}^{M-1} \exp[i\,R_{l\theta}(\mathbf{k}) \cdot \mathbf{r}] - \sum_{l=1}^{M} \exp[i\,S_{l\theta}(\mathbf{k}) \cdot \mathbf{r}] \right\} = \mathcal{N} \sum_{l=0}^{2M-1} (-1)^l \exp\left[i\,f_l^{(D)}(\mathbf{k}) \cdot \mathbf{r}\right] \\
&= \mathcal{N} \sum_{l=0}^{2M-1} (-1)^l \exp\left[i\,\mathbf{k}_l \cdot \mathbf{r}\right].
\end{aligned}
\tag{17}
$$

We call the above $\varphi(\mathbf{r}; \mathbf{k})$ an "incoming" state if $\pi < \beta < \pi + \theta$ for $\beta = \arccos[\mathbf{k} \cdot \hat{\mathbf{x}}]$. We also define $\beta = \pi + \alpha$, so that the incoming condition reads $0 < \alpha < \theta$. Without loss of generality we can set $\mathcal{N} = 1$.

For applications requiring numerical calculations and for which one needs as an "input" (see below) an appropriate waveguide solution characterized by a given $\mathbf{k}$, Eq. (17) is particularly useful since it is written in terms of elementary plane waves instead of the more usual—for this kind of geometry [66]—Bessel functions. But for certain examples next, it will be very handily to express Eq. (17) in polar coordinates, making explicit the symmetries of the system. Such a construction is presented in the Appendix C, leading to

$$
\begin{aligned}
\varphi(\mathbf{r}; \mathbf{k}) &= 2\pi \sum_{n=1}^{\infty} (-i)^{Mn} \varphi_n^{(\theta)}(\alpha)\, \varphi_n^{(\theta)}(\phi)\, J_{nM}(k\rho) \\
&= 2\pi \sum_{n=1}^{\infty} (-i)^{Mn} \varphi_n^{(\theta)}(\alpha)\, \Phi_n(\rho, \phi; k).
\end{aligned}
\tag{18}
$$

Note that $\Phi_n(\rho, \phi; k)$ is the correct nth stationary mode for the $\theta = \pi/M$ wedge waveguide.

IV. TRIANGULAR STRUCTURES WITHIN THE WEDGE WAVEGUIDE

Noninteracting quantum particles confined to cavities are commonly modeled as quantum billiards [5–9,50]: a particle satisfying the Helmholtz equation in a spatially finite region delimited by hard walls of arbitrary shapes, thus with Dirichlet boundary conditions. As pointed out in [62], one advantage of implementing the BWM within waveguide domains is that as a bonus we gain a scheme to solve billiard problems. Indeed, depending on the waveguide geometry, we can assume segments of the waveguide as part of the billiard borders and then

just to consider few $\mathcal{C}_j$ to "complete" the shape, simplifying the numerical calculations.

In our present context, triangles (with one angle given by $\theta = \pi/M$) can be constructed considering only a single straight segment. This is illustrated in Fig. 1(f), for $\mathcal{C}$ forming a right triangle with the sides of the $\theta = \pi/2$ wedge waveguide. Likewise, in Fig. 1(g) either $\mathcal{C}_1$ or $\mathcal{C}_2$ form triangles with one of the angles being $\theta/M < \pi/2$. This can reduce the necessary computational work to obtain the billiard eigenstates. Naturally, if the interest is to investigate a certain structure in the interior of the waveguide, then $\mathcal{C}$ should account for its entire border, as the circle $\mathcal{C}_3$ in the inner region of an acute wedge waveguide [Fig. 1(g)].

TABLE I. Numerical k's for the incident φ's used in Fig. 2. For the triangular billiards with analytical solutions (Appendix D) are also shown the corresponding k_{pq} as well as $\Delta k_\% = |k - k_{pq}|/k_{pq} \times 100\%$ and the ratio $\Delta = |k - k_{pq}|/\overline{\delta}$. N is the dimension of the discretized T matrices.

Fig. 2	Numerical k	k_{pq} (p, q)	$\Delta k_\%$	Δ	N
(a)	15.7142	15.7079 (4,3)	0.040	0.008	84
(b)	102.2942	102.2828 (32, 6)	0.011	0.092	212
(c)	100.0	–	–	–	200
(d)	14.5236	14.5103 (2,0)[a]	0.057	0.008	33
(e)	100.6314	100.6181 $\left(\frac{35}{3}, \frac{11}{3}\right)$[b]	0.013	0.092	210
(f)	100.0	–	–	–	200
(g)	11.0881	11.0824 (6, 2)	0.051	0.008	60
(h)	101.9888	101.9822 (46, 51)	0.006	0.092	620
(i)	100.0	–	–	–	600
(j)	15.7266	–	–	–	68
(k)	101.8605	–	–	–	446
(l)	100.0	–	–	–	438

[a]Symmetry A_1; see Appendix D.
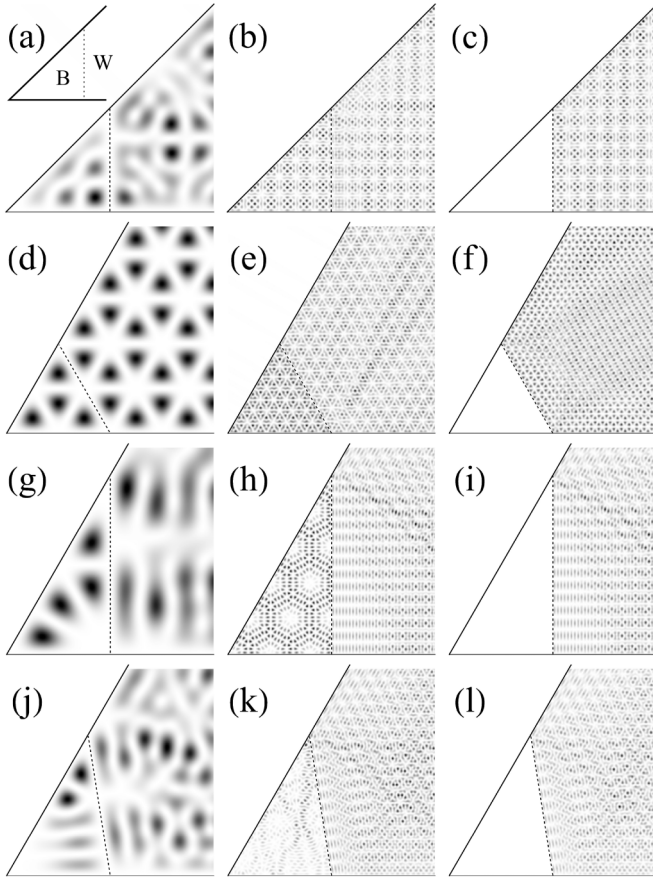[b]Symmetry E; see Appendix D.

FIG. 2. By properly inserting a straight segment $\mathcal{C}$ (dotted lines) within a θ wedge waveguide, it is divided into two distinct regions: a triangular billiard (labeled B) and a waveguide with a wall scatter at its end (labeled W). This is illustrated in the inset of (a). In (a)–(c) $\theta = 45°$ and in (d)–(l) $\theta = 60°$. The resulting billiard shapes are (a)–(c) right $45°$–$45°$, (d)–(f) equilateral, (g)–(i) right $60°$–$30°$, and (j)–(l) $60°$–$\gamma°$–$(120° - \gamma°)$ [with $\gamma = (2 - 3\sqrt{2}/\pi)\,60° \approx 38.97153°$, hence irrational], triangles. For all them, the base side lengths are $\ell = 1$. The density plots correspond to the modulus square of the billiard eigenstates in B—existing depending on k—and of the scattering solutions in W. The darker (lighter) regions indicate a higher (lower) $|\psi|^2$. As it should be, $|\psi|^2$ is null along $\mathcal{C}$ as clearly observed in the plots. The k's of the incident waves considered are listed in Table I. In particular, the k values for the cases displayed in (c), (f), (i), and (l) do not correspond to any eigenwavenumber of the billiards. Therefore, the BWM leads to null ψ's within the related B regions.

To illustrate the protocol, we address representative eigenstates of some triangular billiards as well as their exterior scattering solutions (but, of course, in the interior of the waveguide). Such an approach has already been employed to address the inner quantum states of triangular and trapezoidal perfect cavities in Ref. [62], assuming a rectangular waveguide. Nevertheless, for triangular billiards the θ wedge waveguide is far more suitable once a rectangular waveguide obviously has a distinct symmetry from that of triangles. For instance, supposing rectangular waveguides, one needs to include evanescent modes in the calculations, making the numerical convergence harder (although feasible). Actually, as emphasized in
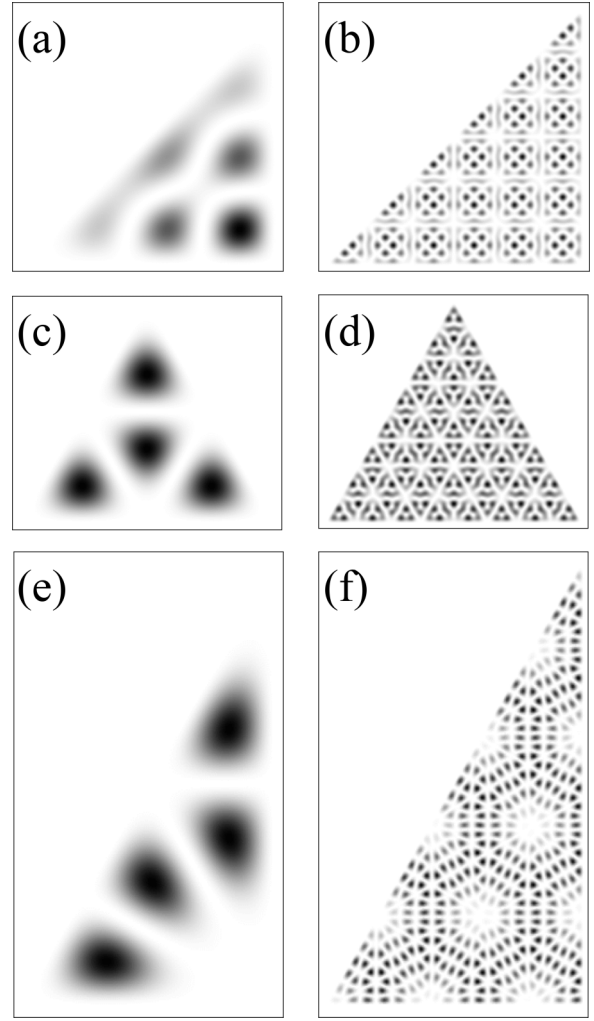

FIG. 3. Density plots of $|\psi_n|^2$ from the analytic solutions in the Appendix D for (a),(b) isosceles, (c),(d) equilateral, and (e),(f) right $60°$–$30°$ triangles. The (a)–(f) eigenstates correspond to the cases (a), (b), (d), (e), (g), and (h) of Fig. 2.

[62], given the specific shape of a billiard one wishes to study, ideally one should choose a waveguide of a complying geometry.

We consider a short segment of line $\mathcal{C}$, which together with the frontiers of a $\theta = 45°$ or of a $\theta = 60°$ wedge waveguide form right isosceles (right $45°$–$45°$), equilateral ($60°$–$60°$–$60°$), right $60°$–$30°$ and $60°$–$\gamma°$–$(120° - \gamma°)$ [with $\gamma = (2 - 3\sqrt{2}/\pi)\,60°$, so irrational] triangles (Fig. 2). In all these examples, the base sides ℓ are set equal to the unity, so the areas A of the triangles are, respectively, $1/2$, $\sqrt{3}/4$, $\sqrt{3}/2$, and 0.6800. Notice that now the structures have two parts, the billiard interior (region B) and the waveguide, but with its wedge tip being substituted by a wall $\mathcal{C}$ (region W); see the inset of Fig. 2(a).

From the BWM, with the Green's function given by Eq. (15) for $\theta = 60°$ and by Eq. (16) for $\theta = 45°$, we display the resulting density plots of $|\psi|^2$ in Fig. 2; the darker regions correspond to the higher values of $|\psi|^2$. Within the billiard, region B, we have the correct eigenstate ψ_n only if the chosen k for the incident φ is equal to the resonance

eigenwavenumber k_n. However, in region W, for any k we get the proper scattering solution associated with φ. As examples of incoming waves, we take φ in Eq. (17) with $\alpha = 3\pi/16$ for Fig. 2(a), $\alpha = \pi/16$ for Figs. 2(b) and 2(c), $\alpha = \pi/6$ for Figs. 2(d) and 2(f), and $\alpha = \pi/12$ for Fig. 2(e) and Figs. 2(g)–2(l). For the k values, we set some representative low $k \sim 15$ ($\ell/\lambda \approx 0.4$) modes, intermediate $k \sim 101$ ($\ell/\lambda \approx 16$) modes and off-resonance k's ($=100$), respectively, in the first, second, and third columns of Fig. 2. The exact numerical values for the k's are shown in Table I.

In particular, the triangular billiards in Figs. 2(b)–2(c), 2(d)–2(e), and 2(g)–2(h) belong to known exactly solvable cases in the literature; e.g., refer to [75–78]. Their analytic expressions are summarized in Appendix D, with the corresponding $|\psi_n|^2$ plotted in Fig. 3. By a direct visual inspection we observe an almost perfect agreement between the morphologies of the ψ_n's from the BWM (Fig. 2) and from the exact formulas (Fig. 3). Although not shown here (but for accuracy analysis, see below), we have also checked that quantitatively, i.e., numerically, the accordance is rather good. We should remark these are just a few illustrations. We have tested an exhaustive number of examples, always finding great concurrence.

Last, inspecting the outside solutions in the region W in Fig. 2, one notices that some extremely regular scattering patterns observed in Fig. 2, e.g., Figs. 2(c) and 2(d), might seem a bit unusual. However, we recall that the incident φ is not a single plane wave in the form $\exp[i\mathbf{k}\cdot\mathbf{r}]$. Instead, it results from the linear combination in Eq. (17). So these special incoming waves, when scattered off by $\mathcal{C}$, give rise to the somehow orderly motifs observed in Fig. 2. In particular, φ in Eq. (17) with the parameter values corresponding to Fig. 2(d) have a nodal line exactly along the loci of $\mathcal{C}$ (just the wall completing the equilateral triangular shape). Therefore, the incoming φ does not "feel" the potential barrier $\mathcal{C}$ and the structure of $|\psi(\mathbf{r})|^2$ everywhere (in both B and W) coincides with that of $|\varphi(\mathbf{r})|^2$. In other words, in this very specific situation, φ restricted to B is already the correct eigenstate of the $60°$–$60°$–$60°$ triangle.

A. Numerical efficiency characterization

Following the same computation schemes comprehensively described in Refs. [49–51,63], the $\mathcal{C}$'s have been divided into N segments, each of length δs. Hence, the necessary number of discretized points N along $\mathcal{C}$ for the T-matrix calculation as well as the ratio $\delta s/\lambda = \delta s\, k/(2\pi)$ are both relevant figures of merit for the method numerical efficiency. Moreover, as aforementioned the exact analytic solutions for the first three types of triangular billiards in Fig. 2 are known (see Appendix D). Then the correct k's (hereafter written as k_{pq}) have been used to check our results' accuracy. So, for the right isosceles, right $30°$–$60°$, and the equilateral triangles we have compared the numerically obtained k's (from the BWM) with the exact k_{pq} (Appendix D), further calculating $\Delta = |k - k_{pq}|/\bar{\delta}$ for $\bar{\delta} = 2\pi/(k_{pq}A)$ the mean level spacing in the vicinity of k_{pq} [79]. A small value for Δ (say <0.1) indicates that the approach properly resolves neighbor levels.

We mention that for the examples analyzed, we have selected the N's so to obtain (i) $\Delta = 0.008$ for low and $\Delta = 0.092$ for intermediate modes for the analytically solvable triangles (repeating the corresponding largest N's for the off-resonance instances), implying in $\delta s/\lambda$ in the range 0.03–0.08 and (ii) $\delta s/\lambda = 0.05$ for the nonintegrable triangular billiard (thus, in this case only demanding N up to 450).

From Table I it is clear that the numerically found resonance k's are quite close to the correct ones. It is worth mentioning that even for the largest N used, 620, the simulations are fast and computationally inexpensive. As a test, we have considered larger N's, around 2000, and all the states ψ obtained were basically the same ones than in Fig. 2, in both B and W. But as it should be, with the corresponding $\Delta k_\%$s further decreasing. For instance, for the state (h) in Table I, for $N = 2000$ one gets $\Delta k_\% = 2.5 \times 10^{-3}$ and $\Delta = 3.6 \times 10^{-2}$.

V. AMPLITUDE GAIN WITHIN WEDGE WAVEGUIDES

For both basic and applied purposes, one could try to determine suitable structures that, when placed in waveguides, would lead to an increase in the amplitude of the internal waves, at least at some specific locations. In fact, as mentioned in the Introduction, there are many theoretical and experimental methods with this goal; see also further remarks in Sec. VI. The aim here is to show that BWM applied to waveguide domains V is a valuable addition to existing methods for searching for such structures.

For our present wedge waveguides, we discuss two different strategies to achieve constructive interference in specific small regions of V, ensuing amplification of the resulting scattering states. Thus, we consider to insert either (1) a leak bulkhead, i.e., a permeable membrane in the form of an arc of a circle, or (2) two hard or permeable wall circular obstacles, near the wedge waveguide acute angle. By playing with the geometrical features of (1) and (2), we can considerably increase the amplitude of the scattering ψ in the region around the waveguide tip.

A. A permeable arc of a circle structure within the θ wedge waveguide

We assume our $\theta = \pi/M$ wedge waveguide with a permeable arc of a circle $\mathcal{C}$ put in its interior, fully surrounding the θ angle region. Such leak bulkhead $\mathcal{C}$ has the parametric equation given by (with $0 < t < \theta$)

$$x(t) = R\cos[t], \quad y(t) = R\sin[t]. \tag{19}$$

From the BWM we are able to derive the exact stationary states for this problem. For so, we first calculate the associated T matrix and then use it to obtain the scattering states for the proposed geometry.

We start supposing θ arbitrary and thus consider the general Green's function in Eq. (7). From Eqs. (3) and (4), we find for our permeable circular arc that

$$T_\gamma^{(j)}(t'', t') = \left(\frac{-i\pi\gamma}{2}\right)^j \sum_{l=1}^{\infty} \varphi_l^{(\theta)}(t'') \varphi_l^{(\theta)}(t')$$

$$\times \left(J_{l\frac{\pi}{\theta}}(kR) H_{l\frac{\pi}{\theta}}^{(+)}(kR)\right)^j. \tag{20}$$
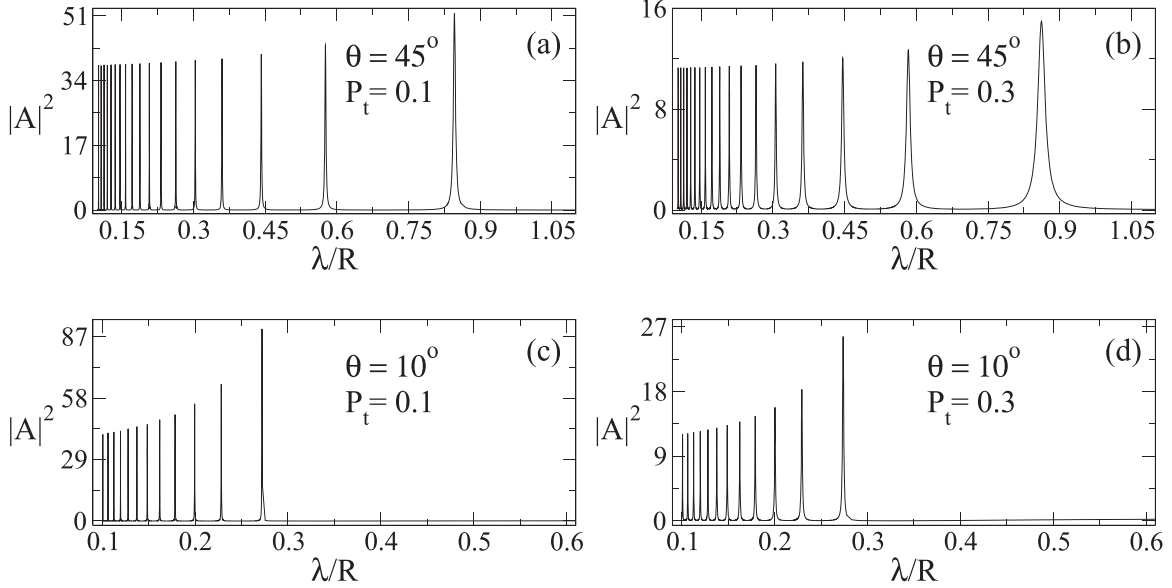
FIG. 4. Modulus square of A given in Eq. (24) as a function of $\lambda/R \geqslant 0.1$ for the fundamental mode $n = 1$ and two values of θ and P_t. To maintain $P_t = 4k^2/(4k^2 + \gamma^2)$ constant, γ assumes different values as $\lambda = 2\pi/k$ varies.

The sum over j can performed exactly, yielding

$$T_\gamma(t'', t') = \sum_{l=1}^{\infty} \frac{\varphi_l^{(\theta)}(t'') \varphi_l^{(\theta)}(t')}{1 + (i\pi\gamma/2) J_{l\frac{\pi}{\theta}}(kR) H_{l\frac{\pi}{\theta}}^{(+)}(kR)}. \quad (21)$$

Above we have used the completeness relation [see Eq. (A2)] for Dirac's delta function.

Now from Eq. (2), $\theta = \pi/M$, $\varphi(\mathbf{r}; \mathbf{k})$ in Eq. (18) and Eq. (21), one has

$$\psi(\mathbf{r}) = 2\pi \sum_{n=1}^{\infty} (-i)^{Mn} \varphi_n^{(\theta)}(\alpha) \psi_n(\rho, \phi; k), \quad (22)$$

where [$\rho_> = \text{Max}(\rho, R)$ and $\rho_< = \text{Min}(\rho, R)$]

$$\psi_n(\rho, \phi; k) = \varphi_n^{(\theta)}(\phi) \Bigg(J_{nM}(k\rho) - i\pi\gamma/2 $$
$$\times \frac{J_{nM}(kR) J_{nM}(k\rho_<) H_{nM}^{(+)}(k\rho_>)}{1 + (i\pi\gamma/2) J_{nM}(kR) H_{nM}^{(+)}(kR)} \Bigg). \quad (23)$$

Each $\psi_n(\rho, \phi; k)$ in Eq. (23) is a correct scattering mode for the $\theta = \pi/M$ wedge waveguide with a permeable ideal membrane (of zero thickness and transparency parameter γ) in the form of an arc of a circle given by Eq. (19).

For the interior region, $r < R$, we have that $\psi_n(\rho, \phi; k) = A_n(k; \gamma) \Phi_n(\rho, \phi; k)$, with Φ_n of Eq. (18) and the amplitude $A_n(k; \gamma)$ reading

$$A_n(k; \gamma) = \frac{1}{1 + (i\pi\gamma/2) J_{nM}(kR) H_{nM}^{(+)}(kR)}, \quad (24)$$

whereas for the exterior region, $r > R$, we get $\psi_n(\rho, \phi) = \Phi_n(\rho, \phi; k) + B_n(k; \gamma) \varphi_n^{(\theta)}(\phi) H_{nM}^{(+)}(k\rho)$, with

$$B_n(k; \gamma) = -\frac{i\pi\gamma}{2} A_n(k; \gamma) J_{nM}^2(kR). \quad (25)$$

In this way, $A_n(k; \gamma)$ is the amplitude change in the standard wedge waveguide mode Φ_n in the region $\rho < R$ around the θ

angle due to the presence of the leak bulkhead. Consequently, if one could properly control the transmissivity (parameterized by γ) through a very thin membrane (see Sec. VI) in the shape of an arc of a circle, the intensity gain nearby the waveguide acute angle would be given by $|A_n(k; \gamma)|^2$.

As mentioned in Sec. III, for a plane wave of wavenumber k incident normally to a point of $\mathcal{C}$, the transmission probability P_t through that point is given by $P_t = 4k^2/(4k^2 + \gamma^2)$. Hence, by supposing distinct γ's for different k's—so to keep P_t constant—we plot in Fig. 4 the modulus square of $A_{n=1}$ (the fundamental mode) as a function of λ/R for $\theta = 45°$ ($M = 4$) and $\theta = 10°$ ($M = 18$) and two values of P_t, namely, 0.1 and 0.3.

Figure 4 illustrates certain general trends identified after testing many parameter values. Large gains, i.e., $|A|^2$ considerably higher than 1, take place for certain particular values of $\lambda/R < 1$. As intuitively expected, the gain tends to be greater for smaller θ's ("tighter" regions) and smaller P_t, thus with the resonance quasibound states becoming more similar to true eigenstates. Moreover, the resonances are narrower in λ for shorter λ and smaller θ and P_t. Finally, the peaks' heights increase with λ. In the present set of examples, the largest gain, of about 91 times, occurs for $\lambda/R \approx 0.27$ in Fig. 4(c). We should observe that the physics underlying all the present results is essentially that related to the emergence of resonance scattering from finite quantum wells in 1D quantum mechanics—for instance, see the nice discussion in [80] as well as a comprehensive example in the Appendix of [51].

We conclude this section remarking that to introduce leaky elements into waveguides to tailor their modes features is not a new idea. For example, it has been used to generate time delay in bandpass filters [81] and to better control beam directivity [82]. However, as far as we know, to use such a simple setup to achieve wave amplitude gain in waveguides has not been properly explored in the literature (refer also to [62]).
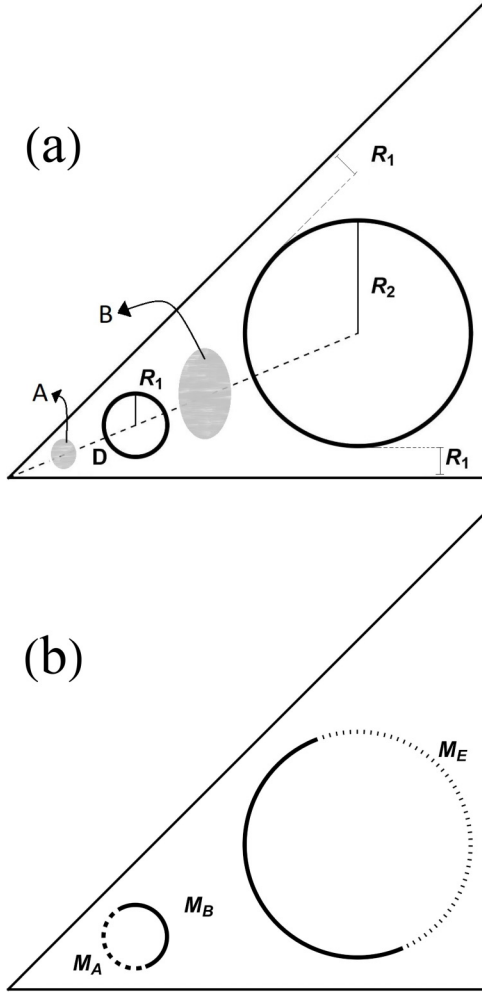
FIG. 5. (a) Two permeable circles of radii $R_1 < R_2$ are placed close to the θ wedge waveguide vertex. Both circles have their centers along the waveguide bisector. The regions to be analyzed for wave amplitude gain are indicated as A (between the vertex and the smaller circle) and B (between the two circles). A relevant characteristic length of the region A (B) is the distance between the waveguide vertex and the smaller circle border, $D - R_1$ [the borders of the two circles, $(R_1 + R_2)(1/\sin[\theta/2] - 1) - D$]. (b) The circles segments used to calculate g (main text): the dashed line (M_A), the full lines (M_B), and the dotted line (M_E).

B. Circular obstacles close to the waveguide vertex

Another possible arrangement to achieve amplitude gain is to set circular obstacles in the region close to the waveguide tip, i.e., near the waveguide vertex. We illustrate this for the $\theta = 45°$ case. We consider two leaky circles, of radii $R_1 < R_2$, with their centers lying along the waveguide bisector, as shown in Fig. 5(a). The distance between the larger circle borders to the two waveguide walls is equal to R_1. The distance of the smaller circle center to the vertex is D. Hereafter, the exterior region E will denote the waveguide portion outward of the vertex, beyond the circle of radius R_2. The goal is to obtain a considerable amplitude enhancement for the scatting state ψ (when compared to the incident φ) in the regions marked as A and B in Fig. 5(a). We observe that a relevant geometric quantity is represented by the

TABLE II. For the cases displayed in Fig. 6, for $C = A, B$ the values of $\mathcal{G}_C$, and d_C, this latter the ratio between the region C characteristic length and the incoming wavelength.

Fig. 6	$\mathcal{G}_A$	d_A	$\mathcal{G}_B$	d_B
(c)	4.2398	1.5750	0.6165	0.2543
(d)	2.3698	1.5456	0.5324	0.3140
(e)	0.2633	1.2715	4.5107	0.5698
(f)	1.2421	1.1541	6.7226	0.6509
(g)	14.0033	1.1119	7.6429	0.6870
(h)	320.5760	1.0946	35.2479	0.7265
(i)	28.7876	1.0680	20.6598	0.8017
(j)	2.5061	0.9973	38.6046	0.8743
(k)	0.3524	0.8418	65.0402	1.0036
(l)	0.1171	0.7143	45.2026	1.1068
(m)	0.0327	0.6066	24.8023	1.1943
(n)	0.0045	0.4606	6.6878	1.3100

characteristic length associated with the region A (B) divided by the incident wavelength $\lambda = 2\pi/k$, given by $d_A = (D - R_1)/\lambda$ [$d_B = ((R_1 + R_2)(1/\sin[\theta/2] - 1) - D)/\lambda$].

For the numerical analysis we set $R_1 = 0.1$, $R_2 = 0.356$, and vary the distance D, the structures' permeability parameter γ, and the incident wavenumber k. We choose the number of discretized points N on the circles so to keep $\delta s/\lambda$ as close as possible to 0.05—a value akin to those in Sec. IV and which leads to good numerical accuracy. Notice that for the BWM, the full wall $\mathcal{C}$ corresponds to the circumferences of the two circles in Fig. 5.

To look for configurations yielding high gains in the aforementioned regions A and B, we consider the BWM scanning procedure developed in [51]. Here we just outline the main idea; for a full account and technical details see [51]. By discretizing the T matrix we have the elements T_{ij}, where in our case the indices $i, j = 1, \ldots N$ run over segments of arc of length δs composing the two circles. A key property of the T matrix [51] (e.g., useful to study the phenomenon of penumbra diffraction in quantum billiards [83]; refer to [50]) is the following. Suppose a small area C nearby [84] to a portion M_C of the wall frontier $\mathcal{C}$. Assume $i, j \in \mathcal{I}_C$ with $\mathcal{I}_C$ the indices associated with the discretization of M_C. Then, if $S_C = \sum_{i,j \in \mathcal{I}_C} |T_{ij}|$ is large, the scattering solution $|\psi|^2$ in the region C tends to have high peaks. In Fig. 5(b) we depict the segments M_A (close to the region A), M_B (close to the region B), and M_E (close to the exterior region) that we are going to use to search for wave amplifications in our setup. Then, for each set of parameter values we calculate $g_C = \log[S_C/S_E]$ ($C = A, B$). Large values of g_C should indicate amplitude gain in C.

For a fixed $\gamma = 50$, $17.5 \leqslant k \leqslant 19$ (so that $0.328 < P_t < 0.366$), and $2.6 \leqslant D/R_1 \leqslant 6.4$, we generate density plots of g_A in Fig. 6(a) and g_B in Fig. 6(b). Darker spots in the graphs represent greater values of g_A and g_B, thus higher wave amplitudes. We shall call connected darker spots forming a kind of trajectory in the $(k, D/R_1)$ space—for instance, in Fig. 6(b) the one similar to a reversed "ξ" letter—a family of scattering resonances. For selected values of k and D/R_1 [always the same pairs in Fig. 6(a) and Fig. 6(b)] we plot in Figs. 6(c)–6(n) the corresponding scattering states $|\psi|^2$
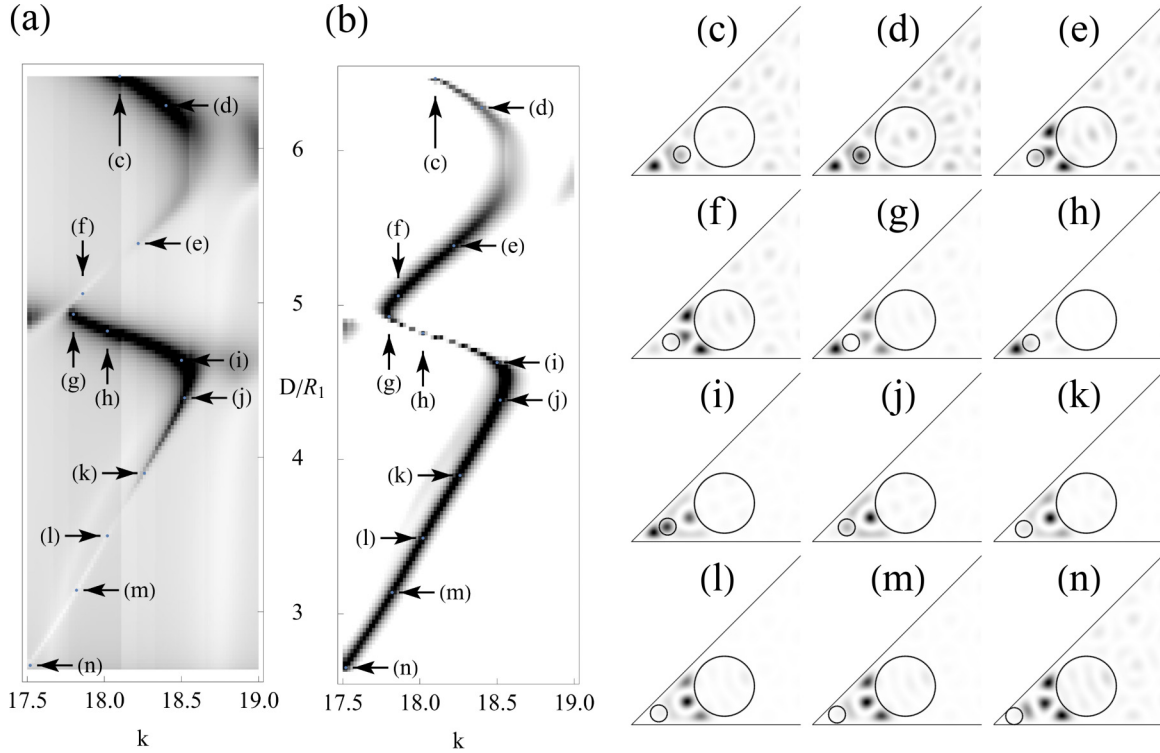
FIG. 6. Density plots of (a) g_A and (b) g_B as function of k and D/R_1 for $\gamma = 50$. For selected values of k and D/R_1 (as indicated), density plots of the scattering solutions $|\psi|^2$ assuming the incident φ with $\alpha = \pi/8$. The specific values of k, D/R_1 are (c) 18.1, 6.46729, (d) 18.40, 6.27787, (e) 18.22, 5.3849, (f) 17.86, 5.06018, (g) 17.8, 4.92488, (h) 18.02, 4.81665, (i) 18.5, 4.62723, (j) 18.52, 4.38369, (k) 18.26, 3.89661, (l) 18.02, 3.49071, (m) 17.82, 3.13894, and (n) 17.52, 2.65186.

assuming $\alpha = \theta/2 = \pi/8$ for the incident wave φ given by Eq. (17).

We emphasize that for the density plots in Fig. 6 we are using a gray scale (with lighter shades representing lower amplitudes). Hence, by qualitatively comparing regions A and B with E, one realizes that although in Figs. 6(c)–6(f) either A or B already presents higher peaks for $|\psi|^2$, they are only a few times greater than those in the exterior region E. On the other hand, for Figs. 6(g)–6(n) the contrast becomes

TABLE III. The same as in Table II but for the scattering states in Fig. 9.

Fig. 9	$\mathcal{G}_A$	d_A	$\mathcal{G}_B$	d_B
(b)	0.0357	1.0868	358.0500	0.7606
(c)	0.0002	1.3110	42.6600	0.6233
(d)	0.0006	1.4144	31.1406	0.5725
(e)	0.0171	1.5857	9.3195	0.5043
(f)	0.00001	0.7507	856.5630	1.1028
(g)	0.0003	0.9762	355.3050	0.9481
(h)	0.0006	1.2149	8.2262	0.8064
(i)	0.0289	1.3551	52.5898	0.7227
(j)	0.0013	0.5165	592.8050	1.3188
(k)	0.0008	0.7031	270.7980	1.1666
(l)	0.0009	0.8806	96.0828	1.0285
(m)	0.6355	0.9761	17 927.5000	0.9643
(n)	3763.2000	1.1580	6094.5300	0.8693
(o)	0.7997	1.2227	211.91900	0.8349

much more pronounced, so the enhancement must be considerably more intense. To better quantify these gains, we define $\mathcal{G}_C = |\psi|^2_{\max,C}/|\varphi|^2_{\max}$, where $|\psi|^2_{\max,C}$ is the maximum of the modulus square of the scattering state ψ in the region C ($C = A, B$) and $|\varphi|^2_{\max}$ is the global maximum of the modulus square of the incoming state φ. For the examples in Fig. 6, the corresponding gains and the spatial parameters d_A and d_B are shown in Table II. Thus, from Table II one sees there is a large diversity of amplifications. For example, it is enormous in A and high in B for Fig. 6(h), considerable in A and B for Fig. 6(i), and to a less extent for Fig. 6(g), and very high in B but absent in A for Fig. 6(k). Regarding the d's, Table II indicates their values are around 1 for both A and B in the cases of higher gains. Nonetheless, for B we should also note that its transversal size—i.e., the distance between the two waveguide walls tangent to the bigger circle—divided by λ is greater, about 2. These linear sizes might be a bit small for certain applications [85–88], but enough for others, as for a nanolens [89–91]. We emphasize the key intention here is just to demonstrate the feasibility of amplitude enhancement using the present type of scatter disposition (see also Sec. VI). A further advancement certainly would be trying to increase the d's, the focus of a forthcoming contribution.

Similar analysis can be performed for other values of γ and larger ranges for k and D/R_1. Thus, assuming increasing γ's, we plot the results for g_A's in Fig. 7 and for g_B in Fig. 8. In such density plots, different families of resonances can be identified. As expected, generally the families in A and B do not need to follow akin trajectories. Indeed, compare the
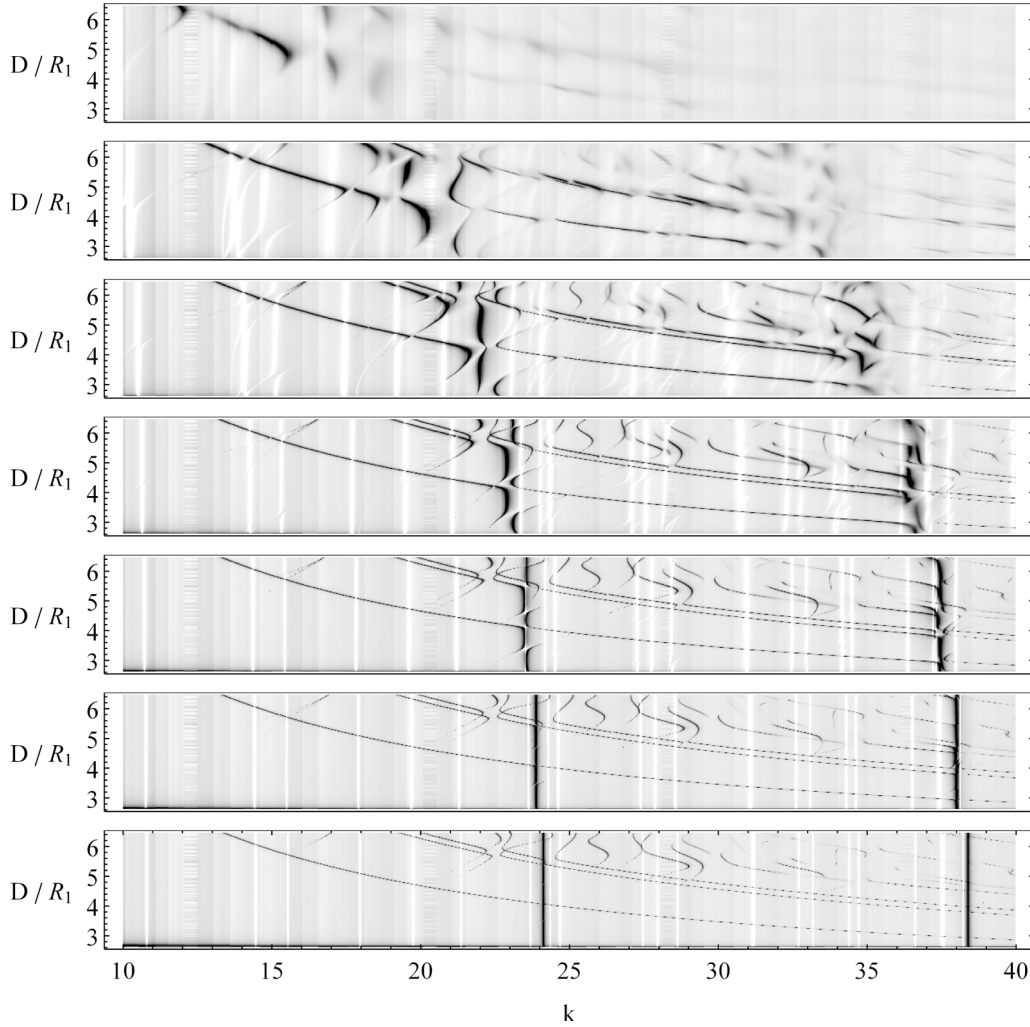
FIG. 7. Density plots of g_A as function of k and D/R_1 for distinct values of γ. From the top to the bottom panels, γ is set to 20 [so that $P_t(k = 25) = 0.862$], 50 [$P_t(k = 25) = 0.500$], 100 [$P_t(k = 25) = 0.200$], 200 [$P_t(k = 25) = 0.059$], 400 [$P_t(k = 25) = 0.015$], 1000 [$P_t(k = 25) = 0.002$], and ∞ (for this last, complete opaque circles, $P_t = 0$). Many amplification resonance families can be clearly identified in the distinct plots as darker lines forming "trajectories" in such a $k \times D/R_1$ space. The lighter vertical lines for greater γ's correspond to the small circular billiard eigenwavenumbers.

"paths" in Figs. 7 and 8. The point is that the spatial geometry of the regions A and B are obviously distinct, therefore the resonance k's usually are not the same.

By inspecting Figs. 7 and 8 one sees that overall the families' trajectories are less fragmented, smoother, and longer when γ increases, i.e., for the circles becoming more opaque. Moreover, for all the graphs in Fig. 7 one can identify the formation of many vertical white lines at specific k's, especially for the larger γ's, whereas in both Figs. 7 and 8, as γ increases two dark vertical lines emerge. The former (latter) patterns correspond to the exact eigenwavenumbers k_n of the bigger (smaller) circle. Actually, since the BWM provides at once the inner eigenstates (if existing) and the outer scattering states of the billiards, the information about their resonances must be contained in the T matrix whenever $k \to k_n$. In fact, the T matrix is exactly the function employed to calculate the g's, hence explaining such motifs.

A relevant question relates to eventual features of the states in a given resonance family. So to investigate the

characteristics of the amplitude gains between the circles (region B) along some families, we consider in Fig. 9(a) a blow up of the intervals $18 < k < 21$ and $2.6 < D/R_1 < 6.4$ for the case $\gamma = 200$ in Fig. 8. Note that for $\gamma = 200$ we have $P_t(k = 20) = 0.0384$. Thus, for the k range in Fig. 9 the circles are almost fully opaque obstacles. Also, greater values of D/R_1 imply spatially closer circles. Particular scattering states along distinct trajectories associated with B are plotted in Figs. 9(b)–9(m). The cases (n) and (o) in Fig. 9(a) are shown in Fig. 10. The corresponding gains in the B (as well as in A for sake of comparison) are shown in Table III.

As a first observation, we notice from the 3D plots in the inset of Fig. 9(a) which g_B oscillates along a trajectory. It implies that the amplitude gains $\mathcal{G}_B$ also vary for the different scattering states throughout a family (refer to the numerical values in Table III). Second, the morphology of the ψ's in a trajectory tend to be similar. For instance, this is the case for the ψ's in the families (I) and (II) in Fig. 9(a)—illustrative
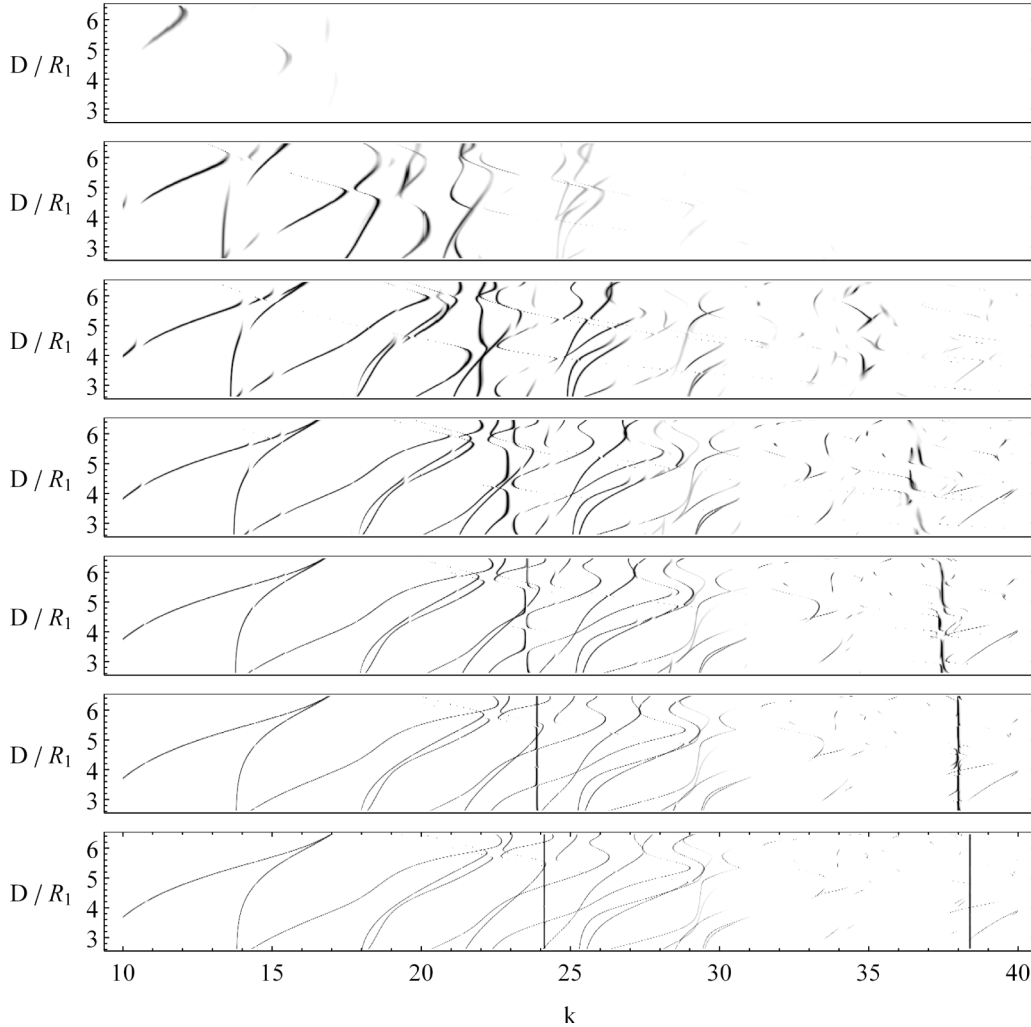
FIG. 8. The same as in Fig. 7, but for g_B. As γ increases (from top to bottom panels), there is the formation of two vertical lines, a behavior also observed in Fig. 7. They correspond to the eigenwavenumbers k_n of the small circle.

$|\psi|^2$ are depicted in Figs. 9(b)–9(e) for (I) and in Figs. 9(f)–9(i) for (II).

However, such a resemblance trend is not mandatory and conceivably should depend on the circles' relative locations and actual values of $\lambda = 2\pi/k$. This becomes apparent for the family (III) of Fig. 9. As an illustration, consider the state (j) with $D/R_1 = 2.79$. For it, the smaller circle is very close to the waveguide vertex, creating enough room for ψ to display three high peaks (all adjacent to the bigger circle) in the region B. But for the state (k), with $D/R_1 = 3.93$, the circles are closer together, and thus two of the previous peaks considerably diminish in B. For D/R_1 increasing even more, there is a rearrangement in the morphology of the ψ's; see Figs. 9(l) and 9(m). Finally, for D/R_1 and k corresponding to (n) and (o) in Fig. 9(a)—which are located to the right of the "gap" in family (III)—we again see three peaks for $|\psi|^2$ [Fig. 10]. But now two of them lying near the smaller circle [compare Fig. 10 with Fig. 9(j)].

All these results exemplify the diverse factors involved in the complex phenomenon of wave amplitude gain in waveguide-like systems. They demonstrate that proper

methods (as the here proposed BWM) are in fact needed to find the right conditions to achieve the effect.

VI. DISCUSSION AND FINAL REMARKS

In this contribution we have employed the BWM—commonly considered to investigate distinct undulatory processes (see the Introduction section)—to study simple setups leading to wave amplitude gain within θ wedge waveguides. For so, an expression for the waveguide Green's function has been derived in the particular case of $\theta = \pi/M$ ($M = 1, 2, 3, \ldots$). Moreover, for billiards whose some sides can be formed by parts of the waveguide walls, the protocol also allows us to obtain the eigenstates of the corresponding closed structures, as demonstrated through explicit computations for triangular shapes. Thus, the present extends the already long list of possible usages for the BWM.

Before addressing few potential applications for the framework, some discussions concerning the physical mechanisms underlying resonances and amplitude enhancement in waveguides are in order. We start observing there is an important
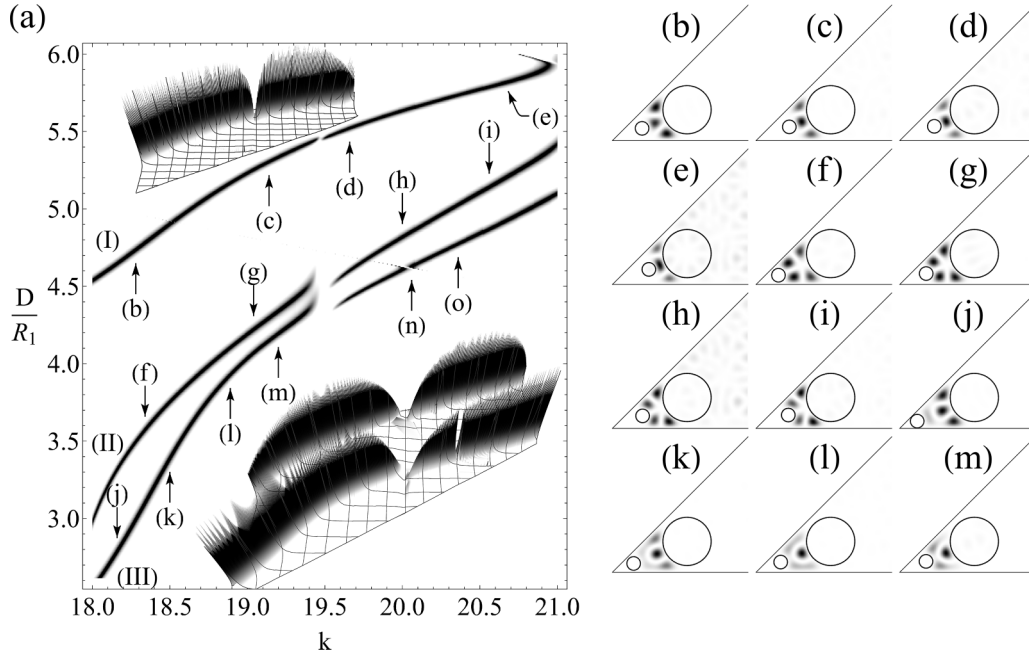
FIG. 9. (a) For $\gamma = 200$, detail of g_B in Fig. 8 in the region $18 < k < 21$ and $2.6 < D/R_1 < 6.4$. It highlights three resonance families, labeled as (I), (II) and (III). In the inset, 3D plots of these three trajectories. For the latter two 3D graphs, an artificial offset has been implemented just to facilitate the visualization. Along the different resonance families, density plots of $|\psi|^2$, corresponding to particular values of the pair $(k, D/R_1)$ (indicated by arrows), are displayed from (b) to (m) [for (n) and (o) see Fig. 10]. The specific values of k and D/R_1 are (b) 18.28, 4.74, (c) 19.14, 5.30, (d) 19.66, 5.52, (e) 20.68, 5.82, (f) 18.34, 3.57, (g) 19.04, 4.22, (h) 20.00, 4.82, (i) 20.56, 5.14, (j) 18.16, 2.79, (k) 18.5, 3.39, (l) 18.89, 3.93, (m) 19.20, 4.19, (n) 20.06, 4.63, and (o) 20.36, 4.77.

literature analyzing changes in the quantum waveguides steady states due to modifications, local [92–95] or not, in their geometry; see [12] and the references therein. Examples of adjustments aimed at controlling the properties of the states in waveguides comprise, e.g., soft [96–101] and sharp [102–104] (including L-shaped [105–107]) bending as well as the introduction of elements of various layouts as cross- and T-junctions [107] and lateral windows [108].

For typical models of straight waveguides, namely, a rectilinear strip of width L and infinite or semi-infinite length [62], the eigenmodes' quantization occurs only in the direction t, transverse to the wave propagation, so that $k_t \sim n_t \pi/L$ with $n_t = 1, 2, \ldots$. On the other hand, in the propagation direction p, we have $k_p \in (0, \infty)$. Then the associated ψ'_{n_t,k_p}s are delocalized states. However, geometrical deformations (local reshaping of the waveguide boundaries) impose extra spatial

FIG. 10. Density plots of $|\psi|^2$ for the states (n) $k = 20.06$, $D/R_1 = 4.63$ (left graph), and (o) $k = 20.36$, $D/R_1 = 4.77$ (right graph) indicated in Fig. 9(a).

modulations to ψ, which for certain special k'_ps might not be accommodated in an extended state. Consequently, we have the formation of bound states [96,102–104] in the continuum. Moreover, the number of such modes are proportional to the deformation strength, e.g., being smaller (greater) for softer (sharper) bending [103,104].

The above phenomenology should likewise hold true for the situations in Sec. V B. Indeed, for these systems the transverse quantization is related to the angular quantum numbers n and the radial is the propagation direction, bearing the wavenumber k [cf. $\Phi_n(\rho, \phi; k)$ in Eq. (18)]. Very importantly, the circles play the role of the local distortions in the waveguide frontiers, altering the morphology of ψ. In this way, the circles when properly placed act as open resonant cavities creating a set of bound states in the continuum [109,110], spatially lying in the regions A and B in Fig. 5. Hence, an incident wave φ with the correct k can excite one of these modes and on top of that inducing a resonator-like effect (see, e.g., [98,103]) giving rise to the observed amplitude gains. It is further emblematic that the obstacles' opacity, gauged by γ, has a direct parallel with the previously mentioned deformation strength. Note from Figs. 8 and 9 that as γ increases we have more bound states since the number of trajectories in the $(D/R_1, k)$ space similarly grows. This is in total accordance with the findings in [103,104] for bent waveguides.

Our contribution can be viewed as a proof-of-concept type of work, illustrating how to utilize the BWM to search for arrangements yielding amplification in waveguide systems. However, final comments related to actual conditions and concrete experimental realizations for the proposed designs are opportune.
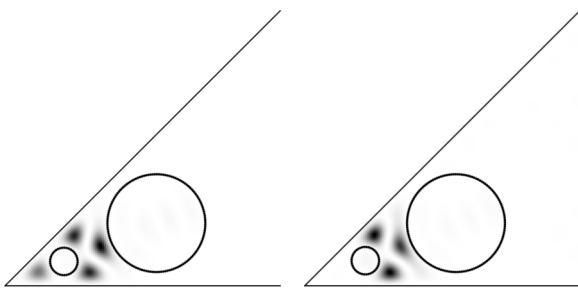
First, the scheme suggested here, i.e., to insert a few structures close to the vertex of wedge waveguides to generate distinct resonant states, can be directly linked to a recently proposed quantum effect [111]. It takes place in confined device systems [112,113], under size-invariant reshaping processes, when the system's geometry is the only one responsible for variations of physical properties, especially thermodynamical. For the examples in Sec. VB, we fix the spatial dimensions, radii of both circles, as well as the position of the outer circle. The cavity format is then changed simply by relocating the inner circle, the kind of transformation proposed in [111]. Thus, our results show that such a quantum shape effect is also possible for nonconfined problems and in principle could also be explored in waveguides.

Second, in the context of matter waves, guiding can be attained, e.g., through deposition of atoms on metallic surfaces, forming distinct array structures [54,55]. More broadly, current quantum engineering permits clever ways to confine, drive, and measure—say, by means of optical-like interferometry—quantum matter (for a review see, for instance, Ref. [7]). Also, several techniques have been developed to fabricate extremely thin membranes, serving as tunneling barriers with various purposes [114–117]. Thence, the specific systems discussed in Secs. VA and VB, in principle representing straightforward theoretical models, may not be too far from real implementations.

Third, relying on certain similarities between the solutions of the Helmholtz equation and TM electromagnetic wave modes, the BWM has been used in the examination of some optical effects (refer to [56,58–60]). Thus, for electromagnetic versions of the situations discussed in Sec. VA (arbitrary P_t) and in Sec. VB (P_t not very small), the leaky walls could be realized by means of dielectric ultrathin films, which can be produced exhibiting different properties and geometries, as mesoscopic hollow spheres [118,119]. For completeness, a relation between our present parameter γ and the characteristics of a very thin dielectric film is presented in the Appendix E. Additionally, if for the two circles in Sec. VB we take the limit $P_t \to 0$, effectively we can assume our obstacles just as opaque disks. Then an actual implementation would be even simpler (see, e.g., the discussion in [60]).

Finally, our approach may also be useful to analyze the important effect of lasing, i.e., amplification of low-intensity electromagnetic waves due to specific features of the optical medium, like the presence of random scatters [48]. Some experimental realizations for these scatters—having different shapes, as spheres [120] and stars [121], and usually made of dielectric materials, like nanodimers [122,123], biomaterials [124], and natural nanofibers [125]—could be used to build a configuration akin to that in Sec. VB—but, of course, with a considerably larger number of obstacles. Presently we are working on an efficient algorithm to simulate much more circles in our wedge waveguide, and hopefully the results will appear in the due course.

The FORTRAN codes to implement the BWM for wedge waveguides and perform all the present simulations are available in a GitHub repository [126].

APPENDIX A: THE GREEN'S FUNCTION FOR AN ARBITRARY θ WEDGE WAVEGUIDE

The present system belongs to a class of problems addressed in [62]. From the results in Sec. 3 of [62], the Green's function for the wedge waveguide can be calculated based on the following general procedure. For $V = (0, \infty) \times \Omega$, with Ω a limited region of $\mathbb{R}^{N-1}$, $\mathbf{r} = (\xi, \boldsymbol{\eta})$, and $[\hat{\mathcal{O}}_\xi = f_2(\xi) \, \partial^2/\partial \xi^2 + f_1(\xi) \, \partial/\partial \xi + f_0(\xi)]$, the Green's function obeying the differential equation

$$
\begin{aligned}
&\left(\nabla_\mathbf{r}^2 + k^2\right) G(\xi, \boldsymbol{\eta}; \xi_0, \boldsymbol{\eta}_0; k) \\
&= \left(\hat{\mathcal{O}}_\xi + f(\xi) \nabla_{\boldsymbol{\eta}}^2 + k^2\right) G(\xi, \boldsymbol{\eta}; \xi_0, \boldsymbol{\eta}_0; k) \\
&= \delta(\mathbf{r} - \mathbf{r}_0) = s(\xi) \, \delta(\xi - \xi_0) \, \delta(\boldsymbol{\eta} - \boldsymbol{\eta}_0), \qquad \text{(A1)}
\end{aligned}
$$

with $G(\xi, \boldsymbol{\eta}; \xi_0, \boldsymbol{\eta}_0; k)|_{\mathbf{r} \in \partial V} = 0$, can be written as $G^{(\pm)}(\xi, \boldsymbol{\eta}; \xi_0, \boldsymbol{\eta}_0; k) = \sum_n w_n(\boldsymbol{\eta}) \, w_n^*(\boldsymbol{\eta}_0) \, F_n^{(\pm)}(\xi; \xi_0; k)$, where

$$
\left(\nabla_{\boldsymbol{\eta}}^2 + k_n^2\right) w_n(\boldsymbol{\eta}) = 0, \quad w_n(\boldsymbol{\eta} \in \mathcal{C}_\Omega) = 0, \quad \int_\Omega d\boldsymbol{\eta} \, w_{n_2}(\boldsymbol{\eta}) \, w_{n_1}^*(\boldsymbol{\eta}) = \delta_{n_2 n_1}, \quad \sum_n w_n(\boldsymbol{\eta}_2) w_n^*(\boldsymbol{\eta}_1) = \delta(\boldsymbol{\eta}_2 - \boldsymbol{\eta}_1),
$$

$$
F_n^{(\pm)}(\xi; \xi_0; k) = C_n^{(\pm)} u_n(\xi_<; k) \, h_n^{(\pm)}(\xi_>; k), \quad C_n^{(\pm)} = \frac{s(\xi_0)}{f_2(\xi_0)} \frac{1}{W[h_n^{(\pm)}(\xi_0; \xi_0; k), u_n(\xi_0; \xi_0; k)]}. \qquad \text{(A2)}
$$

Here $u_n(\xi; k)$ and $v_n(\xi; k)$ are the two fundamental (stationary) solutions of $[\hat{\mathcal{O}}_\xi - f(\xi) k_n^2 + k^2] \, \mathcal{F}_n(\xi; k) = 0$, such that $h_n^{(\pm)}(\xi; k) = \alpha_n u_n(\xi; k) \pm i \beta_n v_n(\xi; k)$ must asymptotically represent an outgoing $+$ (incoming $-$) wave. Further, $u_n(\xi; k)$ is assumed to lead to the same trend of G at $\xi = 0$ and $W[g_2(\xi), g_1(\xi)] \equiv g_2'(\xi) \, g_1(\xi) - g_2(\xi) \, g_1'(\xi)$ is the Wronskian of g_2 and g_1.

In polar coordinates $\mathbf{r} = (\rho, \phi)$, $\nabla_\mathbf{r}^2 = \partial^2/\partial \rho^2 + \rho^{-1} \, \partial/\partial \rho + \rho^{-2} \, \partial^2/\partial \phi^2$ and $\delta(\mathbf{r} - \mathbf{r}_0) = \rho^{-1} \delta(\rho - \rho_0) \delta(\phi - \phi_0)$. Thence, $f_2 = 1$, $f_1 = s = 1/\rho$, $f_0 = 0$, $f = 1/\rho^2$. From Fig. 1(a), $G(\rho, 0; \rho_0, \phi_0; k) = G(\rho, \theta; \rho_0, \phi_0; k) = 0$, and we shall have a well-behaved $G(\rho, \phi; \rho_0, \phi_0; k)$ at $\rho = 0$. Hence, the function w_n in Eq. (A2) is $w_n(\phi) = \varphi_n^{(\theta)}(\phi) = \sqrt{2/\theta} \sin[n\pi \phi/\theta]$, where $k_n = n\pi/\theta$,

and the homogeneous equation for $\mathcal{F}_n$ reads

$$\left\{ z^2 \frac{d^2}{dz^2} + z \frac{d}{dz} + \left[z^2 - \left(\frac{n\pi}{\theta} \right)^2 \right] \right\} \mathcal{F}_n(z) = 0, \text{ with } z = k\,\rho.$$
(A3)

This is the usual Bessel equation [67], whose solutions are the Bessel $J_{\frac{n\pi}{\theta}}(k\rho)$, Neumann $N_{\frac{n\pi}{\theta}}(k\rho)$, and Hankel [of the first $(+)$ and second $(-)$ kind] $H_{\frac{n\pi}{\theta}}^{(\pm)}(k\rho)$ functions of order $n\pi/\theta$. J_ν is regular everywhere with N_ν diverging at the origin. In its turn, asymptotically $H_\nu^{(\pm)}(z) \sim \sqrt{2/(\pi z)} \exp[\pm i\,(z - \nu\pi/2 - \pi/4)]$. Therefore, $u_n(\rho) = J_{\frac{n\pi}{\theta}}(k\rho)$ and $h_n^{(\pm)}(\rho) = H_{\frac{n\pi}{\theta}}^{(\pm)}(k\rho)$. Finally, since

$s(\rho_0)/f_2(\rho_0) = 1/\rho_0$ and $W[H_{\frac{n\pi}{\theta}}^{(\pm)}(k\rho_0), J_{\frac{n\pi}{\theta}}^{(\pm)}(k\rho_0)] = \pm 2i/(\pi\rho_0)$ [66], we obtain Eq. (7).

APPENDIX B: THE PARTICULAR CASE OF $\theta = \pi$

In Sec. III A we have employed the method of images to derive the exact Green's functions for $\theta = \pi/M$ ($M = 1, 2, \ldots$) wedge waveguides. Nonetheless, it would be instructive to see how these expressions can be obtained from the general formula in Eq. (7). This is straightforward for the case of $\theta = \pi$ as we show below.

For $\theta = \pi$, the Green's function is defined in the upper half-plane. So, setting $\theta = \pi$ in Eq. (7), we get (using $\sin[u]\sin[v] = (\cos[u-v] - \cos[u+v])/2$)

$$\begin{aligned} G_\pi^{(\pm)}(\mathbf{r}; \mathbf{r}_0; k) &= \mp i \sum_{n=1}^{\infty} \sin[n\phi]\,\sin[n\phi_0]\,J_n(k\rho_<)\,H_n^{(\pm)}(k\rho_>) \\ &= \mp \frac{i}{4} \left\{ 2 \sum_{n=1}^{\infty} \cos[n(\phi - \phi_0)]\,J_n(k\rho_<)\,H_n^{(\pm)}(k\rho_>) + J_0(k\rho_<)\,H_0^{(\pm)}(k\rho_>) \right. \\ &\quad \left. - 2 \sum_{n=1}^{\infty} \cos[n(\phi + \phi_0)]\,J_n(k\rho_<)\,H_n^{(\pm)}(k\rho_>) - J_0(k\rho_<)\,H_0^{(\pm)}(k\rho_>) \right\}. \end{aligned}$$
(B1)

For $R = |\mathbf{r} - \mathbf{r}_0| = \sqrt{\rho^2 + \rho_0^2 - 2\rho\,\rho_0 \cos[\phi_{\mathbf{r},\mathbf{r}_0}]}$, with $\phi_{\mathbf{r},\mathbf{r}_0}$ the angle between $\mathbf{r}$ and $\mathbf{r}_0$, we have the summation theorem for Bessel functions (8.531-2 in [67]), or

$$\begin{aligned} H_0^{(\pm)}(kR) &= J_0(k\rho_<)\,H_0^{(\pm)}(k\rho_>) \\ &\quad + 2 \sum_{n=1}^{\infty} \cos[n\,\phi_{\mathbf{r},\mathbf{r}_0}]\,J_n(k\rho_<)\,H_n^{(\pm)}(k\rho_>). \end{aligned}$$
(B2)

With the help of Fig. 11, we readily recognize in Eq. (B1) that the terms $\cos[n(\phi - \phi_0)]$ are related to $R = |\mathbf{r} - \mathbf{r}_0|$ and the terms $\cos[n(\phi + \phi_0)]$ to $R_{-\phi} = |\mathbf{r}_{\phi \to -\phi} - \mathbf{r}_0|$. Hence

$$\begin{aligned} G_\pi^{(\pm)}(\mathbf{r}; \mathbf{r}_0; k) &= \mp \frac{i}{4} H_0^{(\pm)}[k|\mathbf{r}(\rho, \phi) - \mathbf{r}_0|] \\ &\quad \pm \frac{i}{4} H_0^{(\pm)}[k|\mathbf{r}(\rho, -\phi) - \mathbf{r}_0|], \end{aligned}$$
(B3)

which is exactly Eq. (9) in Sec. III A by noticing that $\mathbf{r}(x, y) \leftrightarrow \mathbf{r}(x, -y)$ is equivalent to $\mathbf{r}(\rho, \phi) \leftrightarrow \mathbf{r}(\rho, -\phi)$.

APPENDIX C: THE INCIDENT PLANE WAVELIKE $\varphi(\mathbf{r}; k)$, EQ. (17), WRITTEN IN POLAR COORDINATES

The $\varphi(\mathbf{r}; k)$ in Eq. (17) (with $\mathcal{N} = 1$) can be rewritten in polar coordinates via the Jacobi-Anger expansion,

$$\exp[i\,z \cos[\phi]] = \sum_{n=-\infty}^{\infty} i^n \exp[in\phi]\,J_n(z),$$
(C1)

so that [with $\mathbf{k}_l = (k, \beta_l)$ and $\mathbf{r} = (\rho, \phi)$]

$$\begin{aligned} \varphi(\mathbf{r}; k) &= \sum_{l=0}^{2M-1} (-1)^l \sum_{n=-\infty}^{\infty} i^n \exp[in(\beta_l - \phi)]\,J_n(k\,\rho) \\ &= \sum_{n=-\infty}^{\infty} i^n \exp[-in\phi]\,J_n(k\,\rho) \sum_{l=0}^{2M-1} (-1)^l \exp[in\beta_l]. \end{aligned}$$
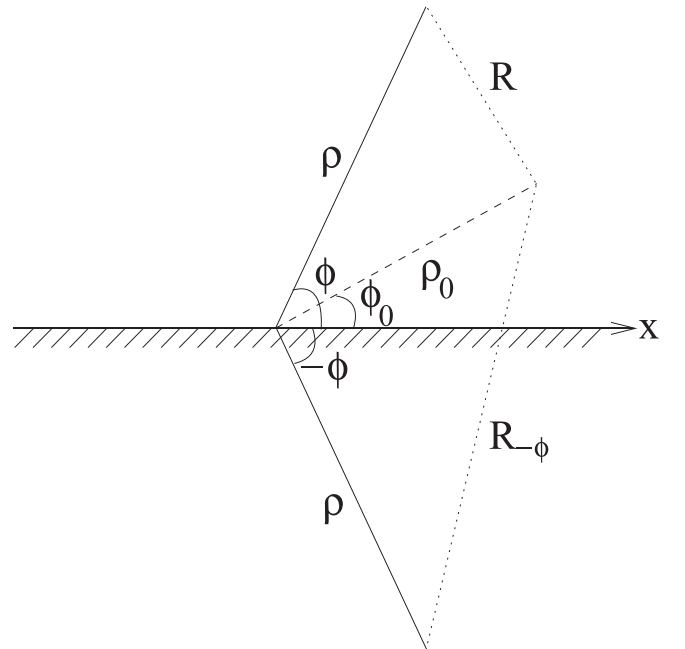(C2)

FIG. 11. The distance between the points (ρ, ϕ) and (ρ_0, ϕ_0), both lying in the upper-half plane, is R. The specular image of (ρ, ϕ) about the x axis is the point $(\rho, -\phi)$, whose distance to (ρ_0, ϕ_0) is $R_{-\phi}$.

Now, recalling the geometric actions of the matrices $S_{l\theta}$ (reflection about the angle $l\,\theta$) and $R_{l\theta}$ (rotation by an angle $2\,l\,\theta$) and the definition of $f_l^{(D)}$, Eq. (13), one finds

$$\beta_l = \begin{cases} +\beta + l\,\theta, & \text{if } l \text{ is even,} \\ -\beta + (l+1)\,\theta, & \text{if } l \text{ is odd,} \end{cases} \quad (C3)$$

which from $\theta = \pi/M$ yields (for m an arbitrary integer)

$$\sum_{l=0}^{2M-1} (-1)^l \exp[in\beta_l] = 2i \sin[n\beta] \sum_{l=0}^{M-1} \exp[2inl\theta]$$

$$= 2i \sin[n\beta]\, M\, \delta_{n\,mM}, \quad (C4)$$

where δ_{pq} is the usual Kronecker's delta.

Next, by inserting Eq. (C4) into Eq. (C2), we get

$$\varphi(\mathbf{r};\mathbf{k}) = \sum_{n=-\infty}^{\infty} i^{nM} \exp[-inM\phi]\, 2i\, \sin[nM\beta]\, M\, J_{nM}(k\,\rho).$$
$$(C5)$$

Finally, since $i^n J_n(k\,\rho)$ is even with respect to n, it reads

$$\varphi(\mathbf{r};\mathbf{k}) = \sum_{n=1}^{\infty} i^{nM} J_{nM}(k\,\rho) \sin[nM\phi]\, \sin[nM\beta]\, 4\,M$$

$$= 2\pi \sum_{n=1}^{\infty} i^{nM} \varphi_n^{(\theta)}(\phi) \varphi_n^{(\theta)}(\beta) J_{nM}(k\,\rho)$$

$$= 2\pi \sum_{n=1}^{\infty} (-1)^{nM} \varphi_n^{(\theta)}(\phi) \varphi_n^{(\theta)}(\alpha) J_{nM}(k\,\rho), \quad (C6)$$

with $\varphi_n^{(\theta)}$ given by Eq. (8) and $\beta = \alpha + \pi$.

APPENDIX D: A BRIEF REVIEW OF THE EXACT SOLUTIONS OF QUANTUM TRIANGULAR BILLIARDS

Three particular triangular billiards treated in this work are the only ones [127] known to have quantum exact analytic solutions; see, e.g., Refs. [75–78,128,129]. They are the right $45°$–$45°$(right isosceles), the right $60°$–$30°$, and the $60°$–$60°$–$60°$(equilateral). In particular, the odd eigenstates through a given bisector of the equilateral triangle correspond to the eigenstates of the right $60°$–$30°$ triangle.

Therefore, recollecting the results in the literature, assuming the spatial orientation for the triangles as in Sec. IV and denoting by ℓ the length of the triangles base sides, we have the normalized eigenstates and eigenwavenumbers as

$90°$–$45°$–$45°$triangle:
$$\psi_{pq}(x,y) = \frac{2}{\ell}\left(\sin\left[\frac{p\pi x}{\ell}\right] \sin\left[\frac{q\pi y}{\ell}\right] - \sin\left[\frac{q\pi x}{\ell}\right] \sin\left[\frac{p\pi x}{\ell}\right] \right),$$
$$k_{pq} = \frac{\pi}{\ell}\sqrt{p^2 + q^2} \quad (p \neq q,\ p,q = 1,2,3,\ldots).$$

$90°$–$60°$–$30°$triangle:
$$\psi_{pq}(x,y) = \frac{2}{\ell}\sqrt{\frac{2}{3\sqrt{3}}}\left(\sin\left[\frac{1}{3}(p-2q)\pi\left(1-\frac{x}{\ell}\right)\right] \sin\left[p\pi\left(1-\frac{y}{\ell\sqrt{3}}\right)\right] \right.$$

$$+ \sin\left[\frac{1}{3}(2p-q)\pi\left(1-\frac{x}{\ell}\right)\right] \sin\left[q\pi\left(1-\frac{y}{\ell\sqrt{3}}\right)\right]$$

$$\left. - \sin\left[\frac{1}{3}(p+q)\pi\left(1-\frac{x}{\ell}\right)\right] \sin\left[(p-q)\pi\left(1-\frac{y}{\ell\sqrt{3}}\right)\right] \right),$$

$$k_{pq} = \frac{2\pi}{3\ell}\sqrt{p^2 + q^2 - pq} \quad (p \neq q,\ p \neq 2q,\ q \neq 2p,\ p,q = 1,2,3,\ldots).$$

$60°$–$60°$–$60°$triangle:
$$\psi_{pq}^{A_{\sigma+1}}(x,y) = \frac{4}{\ell}\sqrt{\frac{1}{3\sqrt{3}(1+\delta_{q0})}}\left(\cos\left[2q\pi\frac{x}{\ell} - \frac{\sigma\pi}{2}\right] \sin\left[\frac{2}{\sqrt{3}}(2p+q)\pi\frac{y}{\ell}\right] \right.$$

$$- \cos\left[2p\pi\frac{x}{\ell} - \frac{\sigma\pi}{2}\right] \sin\left[\frac{2}{\sqrt{3}}(2q+p)\pi\frac{y}{\ell}\right]$$

$$\left. - \cos\left[2(p+q)\pi\frac{x}{\ell} + \sigma\frac{\pi}{2}\right] \sin\left[\frac{2}{\sqrt{3}}(p-q)\pi\frac{y}{\ell}\right] \right),$$

$$k_{pq} = \frac{4\pi}{\sqrt{3}\ell}\sqrt{p^2 + q^2 + pq} \quad (q = \sigma,\sigma+1,\sigma+2,\ldots,\ p = q+1,q+2,\ldots).$$

$$\psi_{pq}^{E,\xi}(x,y) = \frac{1}{\sqrt{2}}\left(\psi_{pq}^{A_2}(x,y) + i\,\psi_{pq}^{A_1}(x,y) \right),$$

$$k_{pq} = \frac{4\pi}{\sqrt{3}\ell}\sqrt{p^2 + q^2 + pq} \quad \left(q = \frac{\xi}{3}, \frac{\xi}{3}+1, \frac{\xi}{3}+2,\ldots,\ p = q+1, q+2,\ldots\right).$$

We observe that the equilateral triangle has a more involved solution, whose symmetry group is C_{3V} of irreducible representations A_1, A_2 (both nondegenerated) and the double degenerated E [76]. Above, σ (ξ) assume the values 0 or 1 (1 or 2).

Using the present exact analytic solutions, the density plots of $|\psi|^2$ corresponding to some cases analyzed in Sec. IV are depicted in Fig. 3. As one readily realizes by contrasting Fig. 3 with the numerical calculations in Fig. 2, the states patterns are exactly the same, illustrating the great accuracy of the waveguide BWM.

APPENDIX E: THE ELECTROMAGNETIC TRANSMITTANCE THROUGH A VERY THIN FILM AND γ

Suppose a nonabsorbing, nonmagnetic thin dielectric film of thickness a and refractive index n embedded in a medium of refractive index n_0. For a monochromatic electromagnetic field (of wavenumber k) incident perpendicular to it, the Fresnel equations for the transmission and reflection waves lead to the following expression for the transmittance through the film ($n_r = n/n_0$) [130,131]:

$$T(k) = \frac{8\,n_r^2}{\left(n_r^2 + 1\right)^2 + 4\,n_r^2 - \left(n_r^2 - 1\right)^2 \cos[2\,k\,n_r\,n_0\,a]}. \quad (E1)$$

Now, if a/λ is small enough such that we can use for the cosine function the expansion $\cos[x] \approx 1 - x^2/2$, then

$$T(k) \approx \frac{1}{1 + \left(n_r^2 - 1\right)^2 [(k\,n_0\,a)/2]^2}. \quad (E2)$$

Finally, by equating $P_t = 4k^2/(4k^2 + \gamma^2)$ to the approximation for $T(k)$ in Eq. (E2), it reads (assuming $n_r > 1$)

$$\gamma = \left(n_r^2 - 1\right) n_0\,a\,k^2. \quad (E3)$$

In this way, given a k, if we wish a certain nonzero P_t—which determines the exact value of γ—ideally the thin dielectric film parameters should be chosen according to Eq. (E3).

In the particular case of large γ, such as some examples in Secs. V A and V B, one should have large $k\,(n_r^2 - 1)/(2n_r)$ to compensate for the fact that $2\,k\,n_r\,n_0\,a$ is small. This might be a challenging condition, but eventually feasible so that the effects observed in Sec. V (for large but not infinite γ) can be achieved from actual thin dielectric films properly placed into electromagnetic waveguides. Of course, for the case of $P_t \approx 0$ for the two circles in Sec. V B, effectively we are not restricted to very thin films—the behavior of the rather small field inside the circles is not really relevant—and the previous practical complications are not an issue.

[1] J. Bonache, G. Zamora, F. Paredes, S. Zuffanelli, P. Aguilà, and F. Martín, Sci. Rep. **6**, 37739 (2016).

[2] B. A. van Tiggelen and S. E. Skipetrov, *Wave Scattering in Complex Media: From Theory to Applications* (Kluwer, Dordrecht, 2003).

[3] J. M. Velázquez-Arcos, J. Granados-Samaniego, and C. A. Vargas, in *Proceedings of the 2013 International Conference on Electromagnetics in Advanced Applications (ICEAA)* (IEEE Xplore Digital Library, New York, 2013), pp. 411–414.

[4] R. Paknys, *Applied Frequency-Domain Electromagnetics* (Wiley-IEEE Press, Hoboken, NJ, 2016), pp. 381–434.

[5] G. Marowsky (ed.), *Planar Waveguides and other Confined Geometries* (Springer, New York, 2015).

[6] J.-P. Connerade, AIP Conf. Proc. **1197**, 1 (2009).

[7] M. Arndt, A. Ekers, W. von Klitzing, and H. Ulbricht, New J. Phys. **14**, 125006 (2012).

[8] K. D. Sen, *Electronic Structure of Quantum Confined Atoms and Molecules* (Springer, Cham, 2014).

[9] J. H. V. Nguyen, P. Dyke, D. Luo, B. A. Malomed, and R. G. Hulet, Nat. Phys. **10**, 918 (2014).

[10] N. Bleistein, *Mathematical Methods for Wave Phenomena* (Academic Press, Orlando, FL, 1984).

[11] R. G. Newton, *Scattering Theory of Waves and Particles*, 2nd ed. (Dover, Mineola, NY, 2013).

[12] P. Exner and H. Kovařík, *Quantum Waveguides* (Springer, Cham, 2015).

[13] B. J. Geurts, F. W. Wiegel, and R. J. Creswick, Physica A **165**, 72 (1990).

[14] R. L. Liboff, Phys. Lett. A **288**, 305 (2001).

[15] B. Schütte, H. Gothe, S. I. Hintschich, M. Sudzius, H. Fröb, V. G. Lyssenko and K. Leo, Appl. Phys. Lett. **92**, 163309 (2008).

[16] E. N. Tsoy, S. Sh. Tadjimuratov, and F. Kh. Abdullaev, Opt. Commun. **285**, 3441 (2012).

[17] Y. Bian, Z. Zheng, X. Zhao, L. Liu, Y. Su, J. Zhu, and T. Zhou, Opt. Commun. **297**, 102 (2013).

[18] S. J. P. Kress, F. V. Antolinez, P. Richner, S. V. Jayanti, D. K. Kim, F. Prins, A. Riedinger, M. P. C. Fischer, S. Meyer, K. M. McPeak *et al.*, Nano Lett. **15**, 6267 (2015).

[19] Z.-Q. Fu, Y. Zhang, J.-B. Qiao, D.-L. Ma, H. Liu, Z.-H. Guo, Y.-C. Wei, J.-Y. Hu, Q. Xiao, X.-R. Mao, and L. He, Phys. Rev. B **98**, 241401(R) (2018).

[20] S. Kumar, K. Chauhan, S. Singh, and D. Foster, Phys. Rev. E **101**, 030502(R) (2020).

[21] R. H. Levi and Y. Kantor, J. Phys. Commun. **6**, 055017 (2022).

[22] L. S. Schulman, Phys. Rev. Lett. **49**, 599 (1982).

[23] C. DeWitt-Morette, S. G. Low, L. S. Schulman, and A. Y. Shiekh, Found. Phys. **16**, 311 (1986).

[24] F. W. Wiegel and P. W. van Andel, J. Phys. A **20**, 627 (1987).

[25] L. Chetouani, A. Chouchaoui, and T. F. Hammann, J. Math. Phys. **31**, 838 (1990).

[26] B. K. Cheng, J. Phys. A **23**, 5807 (1990).

[27] L. Chetouani, A. Chouchaoui, and T. F. Hammann, Phys. Lett. A **161**, 89 (1991).

[28] B. K. Cheng and M. G. E. da Luz, J. Phys. A **25**, 2033 (1992).

[29] H. Razmi and S. M. Modarresi, Int. J. Theor. Phys. **44**, 229 (2005).

[30] H. Jiang, S. Shao, W. Cai, and P. Zhang, J. Comput. Phys. **227**, 6553 (2008).

[31] V. N. Marachevsky and A. A. Sidelnikov, Universe **7**, 195 (2021).

[32] A. Tadeu, P. Santos, and J. António, Comput. Struct. **79**, 1697 (2001).

[33] H. Cao, Waves Random Media **13**, R1 (2003).

[34] C. Dang, J. Lee, C. Breen, J. S. Steckel, S. Coe-Sullivan, and A. Nurmikko, Nat. Nanotechnol. **7**, 335 (2012).

[35] Y. Bian, Z. Zheng, X. Zhao, P. Yang, L. Liu, J. Zhu, and T. Zhou, Opt. Commun. **294**, 414 (2013).

[36] A. E. Miroshnichenko, S. Flach, and Y. S. Kivshar, Rev. Mod. Phys. **82**, 2257 (2010).

[37] C. Li, L. Xu, L. Zhu, S. Zou, Q. H. Liu, Z. Wang and H. Chen, Phys. Rev. Lett. **121**, 104501 (2018).

[38] O. E. Asırım and M. Kuzuoglu, Photonics **7**, 5 (2020).

[39] J. van Ginkel, E. Ruigrok, R. Wentinck, and R. Herber, Front. Earth Sci. **10**, 812658 (2022).

[40] P. Liu, X. Zhang, Z. Ma, W. Cai, L. Wang, and J. Xu, Opt. Express **21**, 32432 (2013).

[41] G. Li, S. Palomba, and C. M. de Sterke, New J. Phys. **21**, 103004 (2019).

[42] W. Lu, L. Viola, K. Pance, M. Rose, and S. Sridhar, Phys. Rev. E **61**, 3652 (2000).

[43] S. P. Shipman, Resonant scattering by open periodic waveguides, in *Wave Propagation in Periodic Media: Analysis, Numerical Techniques and Practical Applications, Vol. 1* edited by M. Ehrhardt (Bentham Science Publishers, Sharjah, 2010), pp. 7–50.

[44] M. H. Nasr, M. A. K. Othman, I. A. Eshrah, and T. M. Abuelfadl, J. Appl. Phys. **121**, 143105 (2017).

[45] P. I. R. Pincheira, A. F. Silva, S. I. Fewo, S. J. M. Carreño, A. L. Moura, E. P. Raposo, A. S. L. Gomes, and C. B. de Araújo, Opt. Lett. **41**, 3459 (2016).

[46] A. S. L. Gomes, E. P. Raposo, A. L. Moura, S. I. Fewo, P. I. R. Pincheira, V. Jerez, L. J. Q. Maia, and C. B. de Araújo, Sci. Rep. **6**, 27987 (1996).

[47] E. P. Raposo, I. R. R. González, A. M. S. Macêdo, B. C. Lima, R. Kashyap, L. de S. Menezes, and A. S. L. Gomes, Phys. Rev. Lett. **122** 143903 (2019).

[48] A. S. L. Gomes, A. L. Moura, C. B. de Araújo, and E. P. Raposo, Prog. Quantum Electron. **78**, 100343 (2021).

[49] M. G. E. da Luz, A. S. Lupu-Sax, and E. J. Heller, Phys. Rev. E **56**, 2496 (1997).

[50] F. M. Zanetti, E. Vicentini, and M. G. E. da Luz, Ann. Phys. **323**, 1644 (2008).

[51] F. M. Zanetti and M. G. E. da Luz, Eur. Phys. J. B **85**, 202 (2012).

[52] J. Nagler, M. Krieger, M. Linke, J. Schönke, and J. Wiersig, Phys. Rev. E **75**, 046204 (2007).

[53] J. A. Katine, M. A. Eriksson, A. S. Adourian, R. M. Westervelt, J. D. Edwards, A. Lupu-Sax, E. J. Heller, K. L. Campman, and A. C. Gossard, Phys. Rev. Lett. **79**, 4806 (1997).

[54] J. Y. Vaishnav, A. Itsara, and E. J. Heller, Phys. Rev. B **73**, 115331 (2006).

[55] J. Y. Vaishnav, J. D. Wall, and E. J. Heller, Phys. Rev. A **76**, 013620 (2007).

[56] A. G. Macedo, F. M. Zanetti, A. Mikowski, J. C. Hummelen, C. M. Lepienski, M. G. E. da Luz, and L. S. Roman, J. Appl. Phys. **104**, 033714 (2008).

[57] H. Garcia-Garcia and J. C. Gutiérrez-Vega, Phys. Rev. E **86**, 016210 (2012).

[58] H. Garcia-Garcia and J. C. Gutiérrez-Vega, J. Opt. Soc. Am. A **31**, 246 (2014).

[59] P. V. Parimi, W. T. Lu, P. Vodo, J. Sokoloff, J. S. Derov, and S. Sridhar, Phys. Rev. Lett. **92**, 127401 (2004).

[60] F. M. Zanetti, L. M. Lyra, F. A. B. F. de Moura, and M. G. E. da Luz, J. Phys. B **42**, 025402 (2009).

[61] A. Nunes, F. M. Zanetti, and M. L. Lyra, Ann. Phys. **373**, 707 (2016).

[62] F. Teston, A. L. Azevedo, M. R. Sales, F. M. Zanetti, and M. G. E. da Luz, J. Phys. A: Math. Theor. **55**, 175201 (2022).

[63] M. R. Sales, A. L. Azevedo, F. Teston, M. G. E. da Luz, and F. M. Zanetti, Chaos **31**, 113122 (2021).

[64] H. M. Macdonald, *Electric Waves* (Cambridge University Press, Cambridge, 1902).

[65] M. A. Nethercote, R. C. Assier, and I. D. Abrahams, Wave Motion **93**, 102479 (2020).

[66] P. M. Morse and H. Feshbach, *Methods of Theoretical Physics* (McGraw-Hill, New York, 1953), Vol. 1.

[67] I. S. Gradshteyn and I. M. Ryzhik, *Tables of Integrals, Series, and Products*, edited by A. Jeffrey and D. Zwillinger (Academic Press, San Diego, 2007).

[68] T. Ehrhardt, A. P. Nolasco, and F. O. Speck, Oper. Matrices **5**, 1 (2011).

[69] T. Ehrhardt, A. P. Nolasco, and F. O. Speck, Oper. Matrices **8**, 301 (2014).

[70] L. P. Castro and D. Kapanadze, J. Math. Anal. Appl. **421**, 1295 (2015).

[71] G. Barton, *Elements of Green's Functions and Propagation* (Oxford University Press, Oxford, 1999).

[72] G. Rowlands, Appl. Sci. Res. **8**, 62 (1960).

[73] C. C. Pinter, *A Book of Abstract Algebra*, 2nd ed. (Dover, Mineola, NY, 2010).

[74] G. Toth, *Glimpses of Algebra and Geometry*, 2nd ed. (Springer, New York, 2002).

[75] W. K. Li, J. Chem. Educ. **61**, 1034 (1984).

[76] W. K. Li and S. M. Blinder, J. Math. Phys. **26**, 2784 (1985).

[77] H. C. Schachner and G. M. Obermair, Z. Phys. B **95**, 113 (1994).

[78] B. J. McCartin, SIAM Rev. **45**, 267 (2003).

[79] M. V. Berry and C. J. Howls, Proc. R. Soc. London A **447**, 527 (1994).

[80] S. C. y. Cruz and O. Rosas-Ortiz, Adv. Math. Phys. **2015**, 281472 (2015).

[81] R. Magnusson, M. S.-Saremi, and X. Wang, Opt. Express **18**, 108 (2010).

[82] N. Memeletzoglou and E. R.-Iglesias, Sci. Rep. **11**, 2260 (2021).

[83] H. Primack, H. Schanz, U. Smilansky, and I. Ussishkin, J. Phys. A **30**, 6693 (1997).

[84] The proper characterization of "close" may be somehow trick in different instances, especially associated with the phenomenon of scattering and diffraction by an obstacle. But since we are already considering a rather small regions of the wedge waveguide, this should not be an issue here.

[85] A. I. Artem'ev, D. N. Klochkov, K. Oganesyan, Y. V. Rostovtsev, and M. V. Fedorov, Laser Phys. **17**, 1213 (2007).

[86] R. Bücker, U. Hohenester, T. Berrada, S. van Frank, A. Perrin, S. Manz, T. Betz, J. Grond, T. Schumm, and J. Schmiedmayer, Phys. Rev. A **86**, 013638 (2012).

[87] T. S. Bird, V. Lingasamy, K. T. Selvan, and H. Sun, IET Microw. Antennas Propag. **11**, 2054 (2017).

[88] G. Nirala, S. T. Pradyumna, A. Kumar, and A. M. Marino, Characterization and control of spatial quantum correlations in entangled light generated via four-wave nixing, in *Frontiers*

in Optics/Laser Science, edited by B. Lee, C. Mazzali, K. Corwin, and R. Jason Jones (Optica Publishing Group, Washington, DC, 2020), paper FM4A.5.

[89] K. Li, M. I. Stockman, and D. J. Bergman, Phys. Rev. Lett. **91**, 227402 (2003).

[90] J. Kneipp, X. Li, M. Sherwood, U. Panne, H. Kneipp, M. I. Stockman, and K. Kneipp, Anal. Chem. **80**, 4247 (2008).

[91] M. I. Stockman, Phys. Today **64**(2), 39 (2011).

[92] M. Andrews and C. M. Savage, Phys. Rev. A **50**, 4535 (1994).

[93] P. Exner and S. A. Vugalter, Lett. Math. Phys. **39**, 59 (1997).

[94] D. Borisov, P. Exner, R. Gadyl'shin, and D. Krejčiřík, Ann. Henri Poincaré **2**, 553 (2001).

[95] G. Cardone, S. A. Nazarov, and K. Routsalainen, ESAIM: M2AN **47**, 305 (2013).

[96] P. Exner and P. Šeba, J. Math. Phys. **30**, 2574 (1989).

[97] P. Exner, Phys. Lett. A **141**, 213 (1989).

[98] F. Sols and M. Macucci, Phys. Rev. B **41**, 11887 (1990).

[99] P. Exner, J. Math. Phys. **34**, 23 (1993).

[100] P. Duclos and P. Exner, Rev. Math. Phys. **07**, 73 (1995).

[101] O. Olendski and L. Mikhailovska, Phys. Rev. B **66**, 035331 (2002).

[102] J. P. Carini, J. T. Londergan, K. Mullen, and D. P. Murdock, Phys. Rev. B **46**, 15538 (1992).

[103] J. P. Carini, J. T. Londergan, K. Mullen, and D. P. Murdock, Phys. Rev. B **48**, 4503 (1993).

[104] S. Bittner, B. Dietz, M. Miski-Oglu, A. Richter, C. Ripp, E. Sadurní, and W. P. Schleich, Phys. Rev. E **87**, 042912 (2013).

[105] P. Exner, P. Šeba, and P. Šťovíček, Czech. J. Phys. B **39**, 1181 (1989).

[106] J. P. Carini, J. T. Londergan, and D. P. Murdock, Phys. Rev. B **55**, 9852 (1997).

[107] D. N. Maksimov and A. Sadreev, Phys. Rev. E **74**, 016201 (2006).

[108] P. Exner, P. Šeba, M. Tater, and D. Vaněk, J. Math. Phys. **37**, 4867 (1996).

[109] C. W. Hsu, B. Zhen, A. D. Stone, J. D. Joannopoulos, and M. Soljačić, Nat. Rev. Mater. **1**, 16048 (2016).

[110] A. Sadreev, Rep. Prog. Phys. **84**, 055901 (2021).

[111] A. Aydin and A. Sisman, Phys. Lett. A **383**, 655 (2019).

[112] A. Sisman, A. Aydin, and J. Fransson, J. Phys. D: Appl. Phys. **53**, 375501 (2020).

[113] A. Aydin, J. Fransson, and A. Sisman, J. Phys.: Condens. Matter **34**, 025301 (2022).

[114] A. Aassime, A. J. Manninen, and J. P. Pekola, Appl. Phys. Lett. **73**, 2369 (1998).

[115] L. F. Buchmann, L. Zhang, A. Chiruvelli, and P. Meystre, Phys. Rev. Lett. **108**, 210403 (2012).

[116] I. Poltavsky, L. Zheng, M. Mortazavi, and A. Tkatchenko, J. Chem. Phys. **148**, 204707 (2018).

[117] C. Henkel, R. Zierold, A. Kommini, S. Haugg, C. Thomason, Z. Aksamija, and R. H. Blick, Sci. Rep. **9**, 6840 (2019).

[118] Z. Hong, W. Dongyanga, F. Yonga, C. Haoa, Y. Yusena, Y. Jiaojiaoa, and J. Liguoa, Mater. Sci. Eng. B **203**, 13 (2016).

[119] D. Mandal, M. Alam, and K. Mandal, Phys. B: Condens. Matter **554**, 51 (2019).

[120] X. H. Wu, A. Yamilov, H. Noh, H. Cao, E. W. Seelig, and R. P. H. Chang, J. Opt. Soc. Am. B **21**, 159 (2004).

[121] J. Ziegler, C. Wörister, C. Vidal, C. Hrelescu, and T. A. Klar, ACS Photonics **3**, 919 (2016).

[122] J. Yan, P. Liu, Z. Lin, H. Wang, H. Chen, C. Wang, and G. Yang, ACS Nano **9**, 2968 (2015).

[123] U. Zywietz, M. K. Schmidt, A. B. Evlyukhin, C. Reinhardt, J. Aizpurua, and B. N. Chichkov, ACS Photonics **2**, 913 (2015).

[124] J. Mysliwiec, K. Cyprych, L. Sznitko, and A. Miniewicz, J. Opt. **19**, 033003 (2017).

[125] S. Kim, S. Yang, S. H. Choi, Y. L. Kim, W. Ryu, and C. Joo, Sci. Rep. **7**, 4506 (2017).

[126] A. C. Maioli, github.com/alanmaioli/wedge/tree/main (2024).

[127] B. J. McCartin, Appl. Math. Sci. **2**, 2891 (2008).

[128] P. Bérard and B. Helffer, Lett. Math. Phys. **106**, 1729 (2016).

[129] R. Samajdar and S. R. Jain, J. Math. Phys. **59**, 012103 (2018).

[130] O. S. Heavens, Rep. Prog. Phys. **23**, 1 (1960).

[131] O. Stenzel, *The Physics of Thin Film Optical Spectra* (Springer, Berlin, 2005).